Effect of Fiber Loading on Mechanical Properties, Friction and Wear Behaviour of Vinylester Composites under Dry and Water Lubricated Conditions

S.R.Chauhan[1], Bharti Gaur[2], Kali Dass[3*]

[1] Asst. Prof., Department of Mechanical Engineering, NIT Hamirpur (H.P.) -177005, India

[2] Asst. Prof., Department of Chemistry, NIT Hamirpur (H.P.) -177005, India

[3] PhD Research Scholar, Department of Mechanical Engineering, NIT Hamirpur (H.P.) -177005,

thakurkalidass999@gmail.com

Abstract-**This paper explores the effect of fiber loading on mechanical properties, friction and sliding wear behaviour of vinylester composites under dry and water lubricated conditions under variation of normal applied loads and sliding speeds. Friction and wear experiments were carried out at ambient conditions on a Pin on disc machine arrangement. From the study it has been found that higher fiber content though improves some of the mechanical properties but also affect adversely some of the properties. The friction and wear properties of vinylester are improved by the addition of glass fiber as reinforced. The coefficient of friction increases with increase in applied normal load and sliding speed under dry sliding condition and decreases with increase in the applied normal load under water lubricated condition, but the specific wear rate for vinylester composites decreases with increase in applied normal load under both dry and water lubricated sliding conditions.**

Keywords-**Vinylester composites; Mechanical properties; coefficient of friction; specific wear rate; SEM**

I. INTRODUCTION

Polymer composites have been increasingly applied as structural materials in the aerospace, automotive and chemical industries, providing lower weight alternatives to traditional metallic materials. A number of these applications are tribological components such as gears, cams, bearings and seals, where the self-lubrication of polymers is of special advantage. One of the features that make polymer composites so promising in industrial applications is the possibility of tailoring their properties with special fillers. Polymers and their composites are emerging as viable alternative material to metal based ones in many common and advanced engineering applications [1-3]. In the industries, the polymers and their composites are being increasingly used in view of their good strength and low densities. Besides, a wider choice of materials and ease of manufacturing make them ideal for engineering applications [4-6].

On account of their good combination of properties, fiber reinforced polymer composites are used particularly in automotive and aircraft industries, the manufacturing of space ship and sea vehicles [7-9]. Fiber reinforced polymer composites are the most rapidly growing class of materials due to their good combinations of high specific strength and specific modulus. Other important characteristics of these materials which make them more attractive compared to conventional metallic systems are low density and ability to be tailored to have stacking sequences that provide high strength and stiffness in directions of high loading [10-12].

Polymer composites consist of resin and a reinforcement two main constituents chosen according to the desired mechanical properties and the application for which they are to be employed [13]. Fibers are the principal constituents in a fibre-reinforced composite material. They occupy the largest volume fraction in a composite laminate and share the major portion of the load acting on a composite structure [14]. Among the fibre reinforcements glass, fibres are widely employed. Polymer composites reinforced with these fibres are usually one to four times stronger and stiffer than their unfilled matrices. It is also well established fact that no material is universally resistant to all modes of wear. Hence during material selection for typical tribo application it becomes imperative to know its complete spectrum of behavior in various possible wearing situations [15]. Glass fibre is also used for the bodies of specialty and sports cars. Glass fibres are electrical insulators, hence their considerable use in laminates for electrical insulation applications [16]. Glass fibers are produced also available in woven form. Varying density woven glass fabrics determine the mechanical properties of fabrics [17].

The role of polymer as a matrix in a fibre-reinforced composite is to transfer stresses between the fibres to provide a barrier against an adverse environment and to protect the surface of the fibres from mechanical abrasion. Glass fibre-reinforced polymer with thermoset polyester resin is an attractive material that is economically desired. Its application at low temperatures and under service terms is easy, when this material is compared to advanced polymer composites with complex molecule structure, high strength and working under terms of difficult service [19].

It is well known that the friction and wear behaviours of polymers in water lubricated condition differ generally from those in the dry sliding condition, and the absorption of water and plasticization of polymer surfaces influence the friction and wear of the polymer [20]. Also the absorption of water can lead to reduction in strength, modulus of elasticity, increase in the elongation and swelling of the surface layer [21, 22]. Lancaster [23] studied the lubrication of carbon fibre-reinforced polymers, and concluded that fluids such as water and other solutions inhibit the formation of transfer films of carbon/ polymer debris on the counter-face and the wear rates are greater than those obtained in dry conditions. In various study of polymer composites with water lubricated sliding conditions reduces the coefficient of friction but may increase the wear rate of the polymer composites [23, 24]. Tanaka et al. [24] investigated the wear behaviour of glass fiber, carbon fiber and carbon bead-reinforced polytetrafluoroethylene (PTFE). The glass-reinforced PTFE showed a very low wear rate with a steel counter face and finally concluded that the fiber preferentially supports the applied load and a fiber rich layer is produced during rubbing action on the mating surface. Unal and Mimaroglu [25] investigated the water lubricated tribological performance of carbon reinforced PEEK composite and they concluded that the coefficient of friction under water lubricated condition is lower than that the dry sliding condition, and he also found that friction and wear behaviour of PEEK composite also lead to a reduction of mechanical efficiency. Therefore the accurate knowledge of the influence of sliding speed and applied load value on the friction and wear is extremely important [26].

In recent years, much research has been devoted to exploring the potential advantage of thermoset matrix for composite applications [27]. One such matrix is vinylester, which has found a place in the family comprising the thermoset engineering polymers due to its excellent mechanical properties with good chemical corrosion resistance. It is also known that vinylester resins bond very well to fiber glass.

Also it is seen from the literature that, a very less amount of work is carried out on mechanical properties, friction and sliding wear behaviour of vinylester composites on a steel disc using a pin-on-disc arrangement under dry and water lubricated conditions. Thus the aim of the present work is to study the effect of fiber loading on mechanical properties, friction and sliding wear behaviour of vinylester composites under dry and water lubricated conditions.

II. EXPERIMENTAL DETAILS

A. Material and Panel Fabrication

In this investigation mechanical and sliding wear of 2D E-glass woven fiber in vinylester matrix composite has been studied. A combination of good mechanical, tribological properties and relatively lower cost of glass fiber makes them an attractive alternative for many engineering applications. The glass fiber chosen is most common type E-Glass fiber (density 2.54 gm/cm^3 and modulus72.4GPa) as reinforcing material in vinylester composites. The glass fabrics are woven in two perpendicular directions. The vinylester resin (density 1.23gm/cm^3 and modulus 2.4-4 MPa) is supplied by Northern Polymer Pvt. Ltd. New Delhi. Methyl ethyl ketone peroxide (MEKP), Cobalt Naphthenate is used as catalyst and accelerator respectively. The woven glass fabrics composites consist of fiber in three different quantities 40 wt%, 50wt% and 60 wt%.

For making of the samples wet hand layup technique is used. The layup procedure consisted of placing the glass sheet on the mould release sheet which has been sprayed by the mould release agent. On this a hardener, accelerator and vinylester resin mixed in required proportion is smeared. Over this, a layer of woven fabric sheet is laid down and resin prepared is spread once again. This procedure is repeated in all three cases unless the required thickness is obtained. A metal roller is used so that air bubbles could be removed and uniform thickness could obtain. After obtaining required thickness, it is covered once again at top by the mould release sheet, sprayed by release agent and smeared with layer of prepared resin. The whole assembly is placed in the mechanical press and pressure is applied and cured at room temperature for 24hours. The sheet prepared of sizes 300mm $\times$ 300mm of required thickness. The details of the composites including weight percentage are shown the Table 1. The test specimens used for tensile, compression, flexural, ILSS, Impact, Hardness and wear tests are cut according to ASTM standards from the respective sheets of fiber percentage 40wt%, 50wt% and 60wt% respectively by sample cutting saw.

B. Mechanical Properties

The Mechanical Properties such as tensile strength, compression strength, flexural strength and inter laminar shear strength (ILSS) were calculated by performing experiments on Hounsefield-25KN universal testing machines as per ASTM standard. The toughness tests were performed on plastic impact tester and hardness was determined on Rockwell hardness tester.

C. Wear Testing and Test Parameters

To evaluate the friction and sliding wear performance of vinylester and its composites of glass fiber reinforced prepared with varying fiber loading under dry sliding condition, wear tests were carried out in a pin-on-disc type friction and wear monitoring test rig (DUCOM) as per ASTM G 99. The counter body is a disc made of hardened ground steel (EN-32, hardness 72 HRC, surface roughness 0.7 μ Ra). The specimen is held stationary and the disc is rotated while a normal force is applied through a lever mechanism. During the test, friction force was measured by transducer mounted on the loading arm. The friction force readings are taken as the average of 100readings every 40seconds for the required period. For this purpose a microprocessor controlled data acquisition system is used.

A series of test are conducted with five sliding velocities of 1.6, 2.2, 2.8, 3.4 and 4m/s under five different normal loading of 10, 20, 30, 40 and 50N. For finding the specific wear, weight loss method was used. During these experiments initial and final weight of the specimens were measured. The material loss from the composite surface is measured using a precision electronic balance with accuracy $\pm$ 0.01 mg. The

specific wear rate (mm^3/N mm) is then expressed on 'volume loss' basis

$$K_s = \frac{\Delta M}{\rho L F_N} \quad (1)$$

Where

K_s- is the specific wear rate ($mm^3N^{-1}mm^{-1}$)

ΔM- is the mass loss in the test duration (gm)

ρ- is the density of the composite (gm/cm^3)

F_{N-} is the average normal load (N).

III. RESULTS AND DISCUSSION

A. *Density and Volume Fraction of Voids*

The theoretical and measured densities along with the corresponding volume fraction of voids are presented in Table 1. It may be noted that the composite density values calculated theoretically from weight fractions which are not in agreement with the experimentally determined values. The difference is a measure of voids and pores present in the composites. It is clear from the Table 1 that increasing fibre content from 40wt% to 60 wt%, there is decrease in void fraction. GV_1 composite has the volume fraction of voids higher compared to other composite specimen GV_2 and GV_3. This may be due to the fact that GV_1 has 60% matrix material which may entrap air during the preparation of composite samples in hand layup technique.

The presence of voids or pores may be due to fibre interaction and fibre constraints on packing in composite laminates. This can affect composite performance adversely which may lead to swelling and reduction in density.

B. *Hardness*

The variation of composite hardness with the weight fraction of glass fibre is shown in Fig. 1. For the composite GV1, the hardness value is recorded as 84HRE while for GV2 as 85HRE and for composite GV3 is measured 87HRE. It is observed that with increase in the fibre content in the composite; improves the hardness, though the increment is marginal. It is well established fact that the strength properties of polymer composites are mainly obtained from the fibre contents and fibre strength. So the variation in the strength of composite with variation of fibre content is obvious.

C. *Tensile and Flexural Strengths*

These variations of composites GV1, GV2 and GV3 in tensile and flexural strengths are shown in Figure 2.

Gradual increase in both the tensile and flexural strength with fibre weight fraction is noticed. Similar observations have been already made for fibre reinforced thermoplastic composites. However it may be mentioned that both these strength properties of the composites are important for structural application.

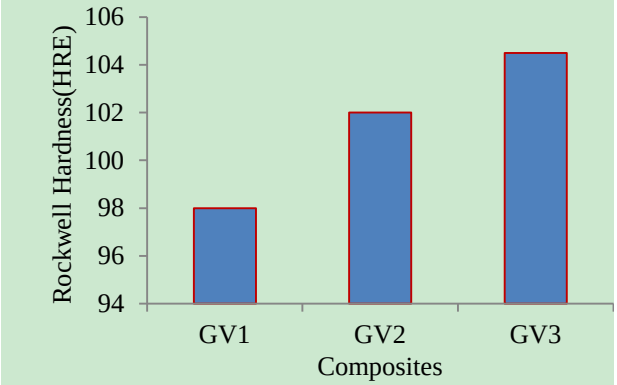

Fig.1 Variation of hardness for composites GV_1, GV_2 and GV_3

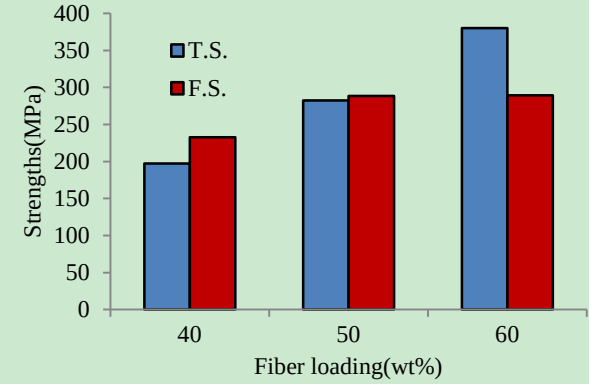

Fig.2 Variation of strengths for composites GV1, GV2 and GV3

TABLE I
MEASURED AND THEORETICAL DENSITY OF THE COMPOSITES (GV_1, GV_2 AND GV_3)

Materials	Composite Specification	Measured Density(gm/cc)	Theoretical density(gm/cc)	Volume fraction of voids (%)	Load (N)	Sliding speed(m/s)
GV_1	(Vinylester+40wt% glass fibre)	1.95	2.24	10.02	10 20 30 40 50	1.6 2.2 2.8 3.4 4.0
GV_2	(Vinylester+50wt% glass fibre)	2.25	2.36	4.58	10 20 30 40 50	1.6 2.2 2.8 3.4 4.0
GV_3	(Vinylester+60wt% glass fibre)	2.88	2.95	3.67	10 20 30 40 50	1.6 2.2 2.8 3.4 4.0

D. Inter Laminar Shear Strength (ILSS)

When a short beam is subjected to three points bending, the maximum shear stress (Interlaminar shear stress) occurs in the beam mid plane (neutral plane) where normal stresses are zero. This results in combination of failure modes, such as fibre rupture, micro buckling and interlaminar shear cracking. The maximum bending stresses (compression and tensile) occur at the beam upper and lower surfaces. The ratio (maximum shear stress / maximum bending stresses), increases as the beam span length to thickness ratio decreases, and thus the beam is more likely to fail in shear. An isotropic material in bending will fail in shear if (maximum shear stress / maximum bending stress), exceeds 0.58 according to the Von Mises criterion. Anisotropic materials may fail in shear at a lower (maximum shear stress / maximum bending stress) ratio. Since there is no guarantee that the specimen in a short beam shear test will fail in shear, the calculated value is referred to as the apparent interlaminar strength, which is a lower bound estimate to the interlaminar shear strength. Interlaminar shear strength depends primarily on the matrix properties and fibre matrix interfacial strength rather than fibre properties. ILSS can be improved by increasing the matrix tensile strength and matrix volume fraction. The glass fabric composite samples showed similar responses to those observed in three point bending. The failed specimen shows that the glass fibre sample did not reveal interlaminar failure. All these observations suggest that the glass fabric reinforced samples failed in bending in the SBS tests.

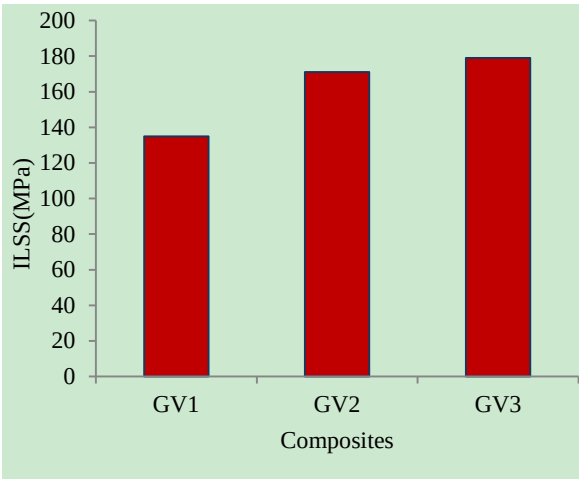

Fig. 3 Variation of ILSS strength for composites GV_1, GV_2 and GV_3

In the present work the ILSS values are measured for glass vinylester composites GV_1, GV_2 and GV_3 and an improvement is recorded in ILSS values with increase in the fibre content in them. Values are illustrated in the Figure 3.

E. Impact Strength

The study of impact behaviour of fibrous composite materials is an essential requirement before recommending for structural and engineering applications. The strength of matrix, fibre strength, orientation and weight fraction significantly influence the impact strength of the glass fibre vinylester composites. In the present investigation since the orientation is kept same in all three composite samples, the difference in the impact energy values will be due to the fibre content. The variation is shown in Figure 4.

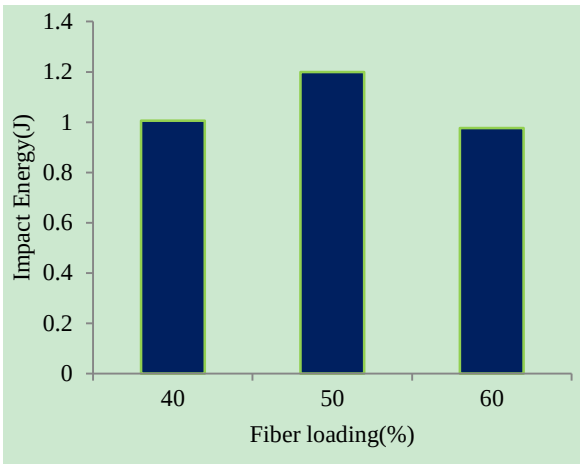

Fig. 4 Variation in impact energy for composites GV1, GV2 and GV3

A significant increase in impact strength is observed for increasing the fibre content from 40wt% to 50wt%. However with increasing the fibre content beyond this to 60wt%, there is decrease in the impact strength. Similar results have been reported in the earlier research. This fact can be considered a high content of fibres, poor dispersion and distribution of the fibres in the matrix. It seems that 50wt% of fibers is the limiting value to increase the impact properties of vinylester based composites. However at very high wt% of fibers, the role played by matrix to distribute the stresses developed is nullified and thus the failure becomes easier.

F. Wear Measurement

In this section friction and sliding wear characteristics of pure vinylester (V) and E-glass fibre vinylester composites GV_1, GV_2 and GV_3 under different applied normal loads and sliding speeds under dry sliding conditions are evaluated. Table 1 presents the physical properties and test conditions for the evaluation of coefficient of friction and specific wear rate of vinylester (V) and glass vinylester composites, GV_1, GV_2 and GV_3.

G. Effect of Normal Load and Sliding Speed on Coefficient of Friction

The experimental results for coefficient of friction for glass vinylester composites GV_1, GV_2 and GV_3 tested under normal loads of 10, 20, 30, 40 and 50N and sliding speeds of 1.6, 2.2, 2.8, 3.4 and 4m/s are shown in Figs. 5(a-c).

Figs 5(a-c) shows the variation in coefficient of friction with applied normal load under both dry and water lubricated sliding conditions.

From the Figs. 5(a-c) shows that the coefficient of friction increases with increase in applied normal load under dry sliding condition and decreases with increase in the applied normal load under water lubricated condition. Under all the test conditions the maximum coefficient of friction was found to be for vinylester composites GV_1 at sliding speed of 4 m/s and applied normal load of 50N under dry sliding condition,

and minimum at sliding speed of 1.6 m/s and applied normal load of 50N under water lubricated dry sliding condition. Also from the Figs. 5 (a-c) it is observed that coefficient of friction increases with increase in sliding speed under both dry and water lubricated sliding conditions. The difference in coefficient of friction values between water lubricated and dry sliding conditions has an average of 56.55%. The mean overall difference is about 57%. But when the applied normal load increases to the limit load values of the polymer the friction will increase due to the critical surface energy. Further it can be explained as the frictional power increases the temperature of the steel surface, which leads to relaxation of polymer molecule chains and bond at fibre-matrix gets weakened. Due to which fibres are broken into fragments and form debris with matrix particles. Higher the glass fibre present in matrix more is the frictional resistance in dry sliding condition. Generally the coefficient of friction for vinylester and glass vinylester composites under water lubricated sliding conditions is lower than the dry sliding conditions. These reductions in coefficient of friction values are attributed to the part which water plays as lubricant. The presence of water at the interface of specimen and steel disc washes away the wear debris. This improves the thermal properties of specimen considerably and also this results into assisting of the occurrence of h ydrodynamic contact full film thickness.

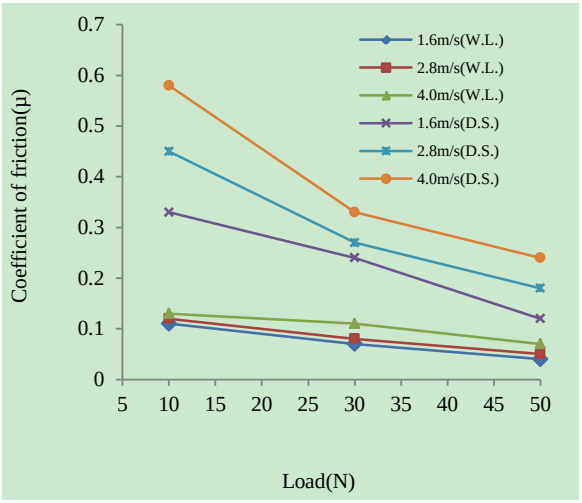

(a)

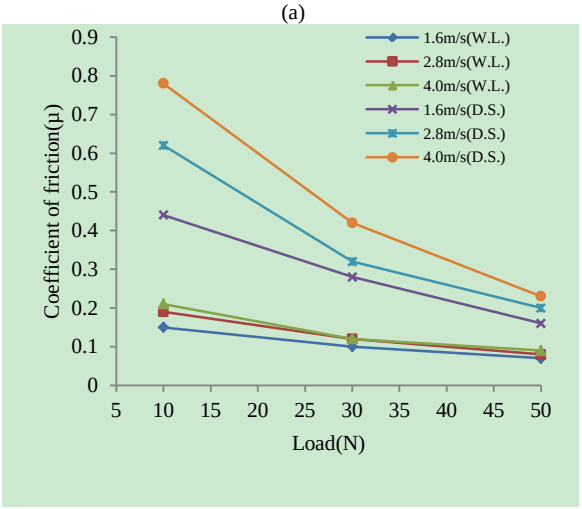

(b)

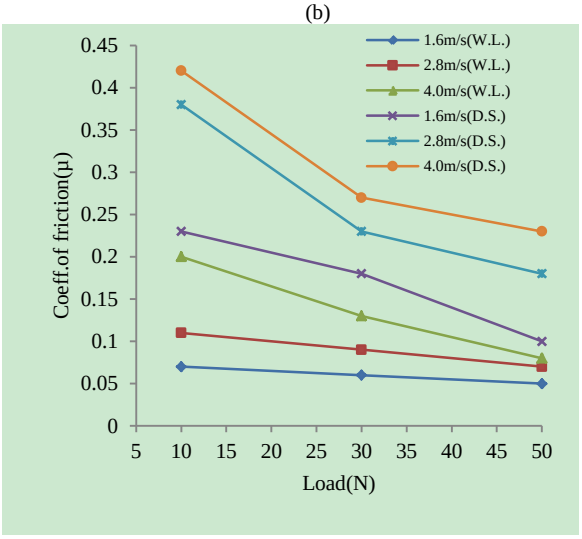

(c)

Figs. 5 (a-c) Variation of coefficient of friction with normal load under dry and water lubricated sliding conditions (a) GV_1 (b) GV_2 and (c) GV3

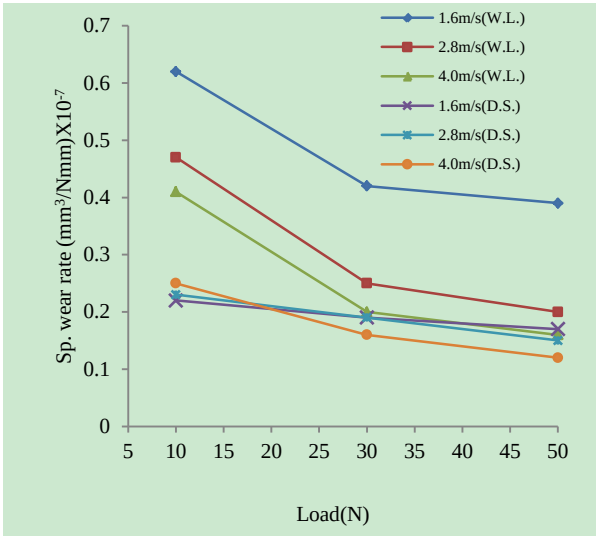

(a)

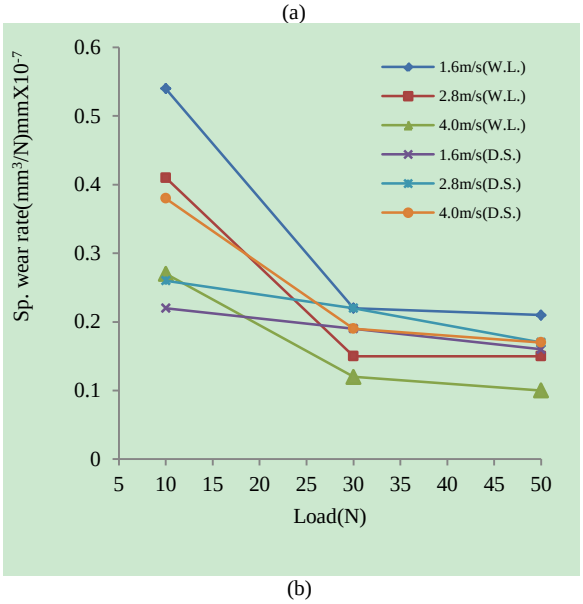

(b)

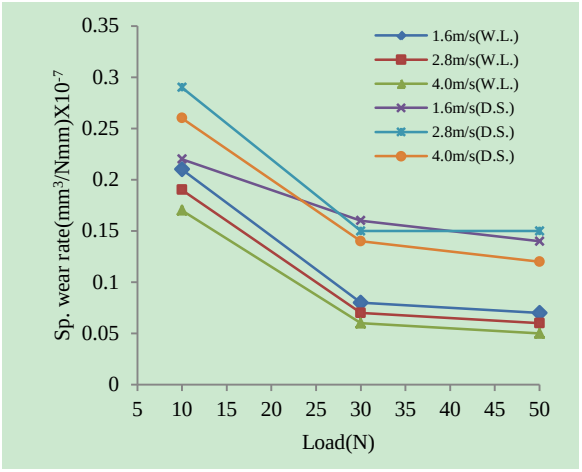

(c)

Figs. 6 (a-c) Variation in specific wear rate with applied normal load under dry and water lubricated conditions sliding condition (a) GV1 (b) GV2 (c) GV3

H. Effect of Applied Normal Load and Sliding Speeds on Specific Wear Rate

The specific wear rate values calculated from mass loss of E-glass fibre reinforced vinylester composites (GV_1, GV_2 and GV_3) tested under different testing conditions of load 10, 20, 30, 40 and 50N and speeds of 1.6, 2.2, 2.8, 3.4 and 4.0 m/s are shown in Figs. 6 (a-c).

The Figs. 6 (a-c) shows the variation of specific wear rate with applied normal load and sliding speeds under both dry and water lubricated sliding conditions. From Figs. 6 (a-c) it is evident from these figures that in this investigation within load range of 10N-50N, the specific wear rate is influenced by increasing the applied normal load and the sliding speeds. From the Figs. 6 (a-c) shows that the specific wear rate for vinylester composites decreases with increase in applied normal load under both dry and water lubricated sliding conditions. The Fig. 6 (a) shows that specific wear rate of glass vinylester composite GV_1 under water lubrication condition is higher than the dry sliding condition.

It is also noticed that under water lubrication sliding condition the specific wear rate decreases with increase in sliding speed. At lower sliding speeds there are differences in specific wear rates. From the Fig. 6 (b) it is observed that there is marginal difference in the specific wear rate for both under water lubricated and dry sliding conditions of composite GV_2. From the Fig. 6 (c) the observations show that the specific wear rate is lesser in water lubricated sliding condition than dry sliding condition of composite GV_3. It is also noticed that with increase in sliding speed the specific wear rate decreases. This is explained by the film layer formation on counter face in dry sliding conditions whereas in water lubrication this layer is removed and fresh composite surface is ready for sliding under water lubricated condition.

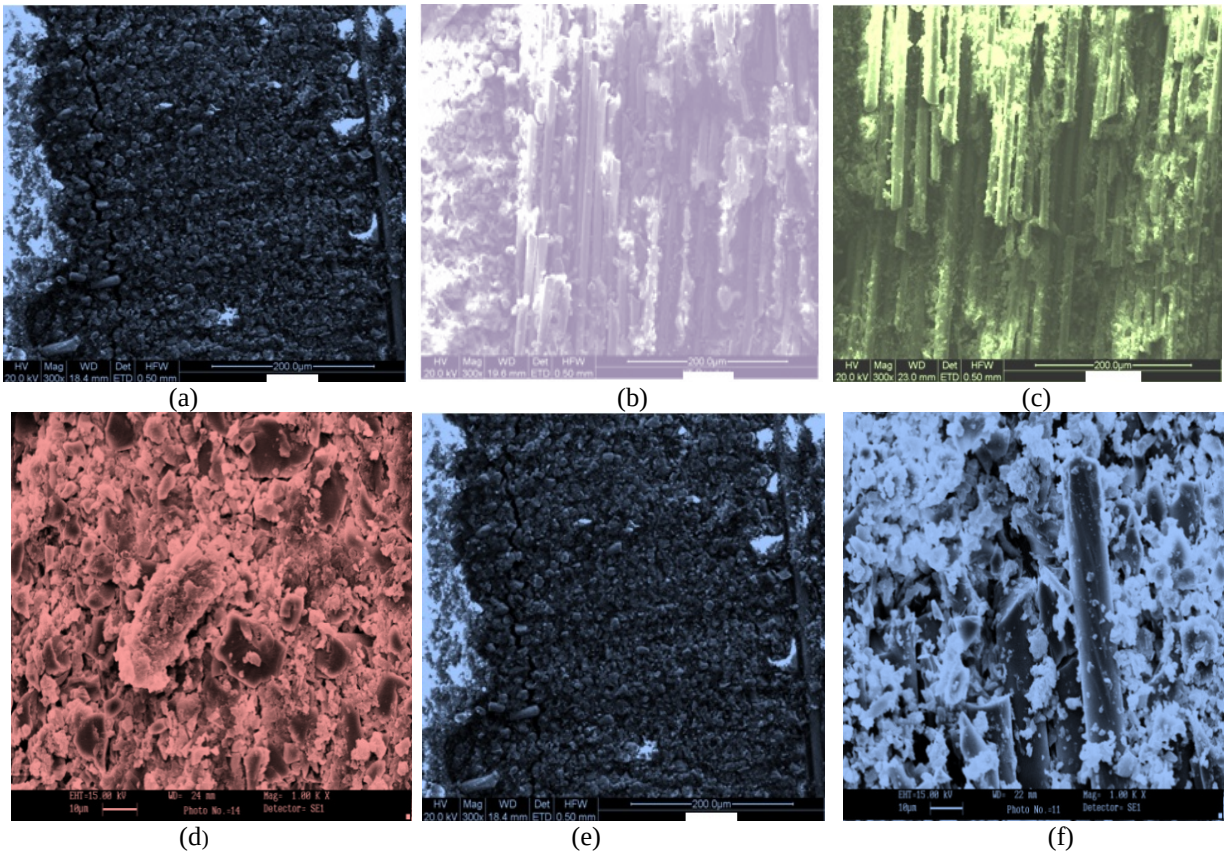

(a) (b) (c)

(d) (e) (f)

Figs. 7 SEM pictures of vinylester composites at 50N load and 4.0 m/s sliding speed under dry sliding (a) GV_1 (b) GV_2 (c) GV_3 and water lubricated conditions (d) GV_1 (e) GV_2 (f) GV_3.

Water prevents the formation of the transfer films of the fibre glass/vinylester matrix on the counterface by removing the debris [8].

The specific wear rate under water lubrication condition is close to those obtained in dry sliding conditions. More over the frictional heat loosens the bond between fibre and matrix due to thermal relaxation, which causes the loss of weight in dry sliding conditions. However in case of water lubricated conditions the effect of thermal penetration is avoided by cooling effect by the presence of water at interface of the composite specimen and steel disc. The fibre content also affects the wear behaviour of the glass vinylester composites. The composite GV_3 with 60wt% E-glass fibre reinforcement shows more compact bond and does not allow the polymer particles to wear out easily. Hence higher fibre content shows low wear loss particularly at higher sliding speeds.

I. Scanning Electron Microscopy

Typical SEM features of worn surfaces of E-glass vinylester composites GV_1, GV_2 and GV_3 at applied normal load of 50N and sliding speed of 4.0m/s are shown in figure 7. (a-f) under dry and water lubricated sliding conditions.

The surfaces of the specimens were examined directly by scanning electron microscope JEOL JSM-6480LV. The composite samples were mounted on stubs with silver paste. To enhance the conductivity of the samples, a thin film of platinum was vacuum-evaporated onto them before the photomicrographs are taken. The specific wear rate data in respect of selected samples is hereby discussed based on scanning electron microscopic features. Figure 7 (a) presents the features of worn surface of GV_1 composite specimen at applied normal load of 50N and sliding speed of 4.0m/s under dry sliding conditions.

From the surface the uniform distribution of matrix with small cracks, debris formation and very small amount of fibre exposure can be observed. SEM picture shown in figure 7 (d) presents the features of worn surface under water lubricated sliding conditions of composite GV_1 at applied normal load of 50N and sliding speed of 4.0m/s and it is observed that matrix is well spreaded and covering the fibres. This shows the smaller amount of wear in the presence of water as lubricant. Similarly the figures 7 (b) and 7 (e) present the SEM features of composite GV_2 under dry and water lubricated sliding conditions at applied normal load of 50N and sliding speed of 4.0m/s respectively. It is observed that under dry sliding condition fibre breakage, debris formation and fibre exposure depicting higher wear rate than under water lubricated conditions representing the fibre exposure with very small amount of matrix sticking to fibre only and effects of water acting as coolant and lubricant are seen. Figures 7 (c) and 7 (f) represent the worn surface features of composite specimens GV_3 under dry and water lubricated sliding conditions at applied normal load of 50N and sliding speed of 4.0m/s respectively.The observations of these surface show that wear of tested composite is lesser under water lubricated conditions. From this study it is noticed that increasing fibre contents in vinylester composites there is considerable reduction in specific wear rate. The effect of load is more pronounced on composite specimens than the sliding speeds.

IV. CONCLUSIONS

The following conclusions can be drawn from the present study:

- The density of the composite specimens is affected marginally by increasing the fiber content.

For the composites with higher percentagee of fiber content, cured at room temperature shows slight increase in density.

- Incorporation of higher percentage beyond 50% fiber loading to 60% has improved the tensile strength, tensile modulus and elongation. For 50% fiber reinforcement, composite laminates have maximum values for the flexural strength, ILSS strength but there is reduction in these properties when fiber content is increased further to 60%. The compression strength also reduced with increase in fiber content from 40% to 50% & 60% for the specimen.

- The coefficient of friction increases with increase in applied normal load and sliding speed under dry sliding condition and decreases with increase in the applied normal load under water lubricated condition, but the specific wear rate for vinylester composites decreases with increase in applied normal load under both dry and water lubricated sliding conditions.

- The response to friction and dry sliding wear in vinylester is influenced considerably

by the addition of woven bi-direction glass fiber as reinforcement and its amount also. The variation in the fiber content attempted in this work, exhibit lower wear loss compared to pure vinylester resin. This is due the reason that pure vinylester has small mechanical properties.

Therefore vinylester with fiber reinforcement improves load carrying capability that lower the wear rate. Also higher amount of glass fiber reinforcement reduces the specific wear rate.

- Wear study against Hardened grounded steel disc counterface under various loads and sliding speeds, the wear performances of vinylester and glass fiber reinforced composites with varying fiber loading are ranked as follow.

GV_3(Vinylester+60%GFR)>GV_2(Vinylester+50%GFR)>GV_1 (Vinylester+40%GFR) > V (Pure Vinylester) (K_S in the order of $10^{-8}mm^3N^{-1}m^{-1}$) and can be considered as a very good tribo material. The results are comparable to the epoxies and other tribo materials.

REFERENCES

[1] AS M Handbook, ASM international, Materials, Park, USA, 18,1992.

[2] L. Chang, Z. Zhang, C. Breidt, K. Friedrich, Tribological properties of epoxy nanocomposites: I. Enhancement of the wear resistance by nano-TiO2 particles, Wear 258 (2005) 141–148.

[3] L. Chang, Z. Zhang, Tribological properties of epoxy nanocomposites: II. A combinative effect of short fibre with nano-TiO2, Wear 260 (2006) 869–878.

[4] Kishore, P. Sampathkumaran, S. Seetharamu, A. Murali, R.K. Kumar,J. Reinforced Plastics and Composites 18 (1) (1999) 55–62.

[5] Kishore, P. Sampathkumaran, S. Seetharamu, S. Vynatheya, S.Murali, R.K. Kumar, SEM observations of the effects of velocity and load on the sliding wear characteristics of glass fabric–epoxy composites with different fillers, Wear 237 (2000) 20–27.

[6] A.A. Collyer, Rubber Toughened Engineering Materials, Chapman & Hall, London, 1994.

[7] H. Pıhtılı, N. Tosun, Investigation of the wear behaviour of a glass fibre-reinforced composite and plain polyester resin, Composite Sci. Technol. 62 (3) (2002) 367–370.

[8] N.S. El-Tayep, R.M. Gadelrap, Friction and wear properties of E-glass fiber reinforced epoksi composites under different sliding contact conditions, Wear 192 (1996) 112–117.

[9] M.T. Mathew et al. Tribological properties of the directionally oriented warp knit GFRP composites; Wear 263 (2007) 930–938.

[10] N. Chand, A. Naik, S. Neogi, Three-body abrasive wear of short glass fibre polyester composite, Wear 242 (2000) 38–46.

[11] I.M. Hutchings, Tribology; Friction and Wear of Engineering Materials, CRC Press, London, 1992, pp. 156–162.

[12] A.P. Harsha, U.S. Tewari, Polym. Test. 21 (2002) 697–709.

[13] M.R. Piggot, Load-Bearing Fibre Composite, Pergamon Press,Oxford, 1980.

[14] S.N. Kukureka, C.J. Hooke, M. Rao, P. Liao, Y.K. Chen, The effect of fibre-reinforcement on the friction and wear af polyamide 66 under dry rolling–sliding contact, Tribol. Int. 32 (1999) 107–116.

[15] Bijwe J, Indumathi J, John Rajesh J, Fahim M (2001) Wear 249:715

[16] P.K. Mallick, Fiber-Reinforced Composites: Materials, Manufacturing, and Design, Marcel Dekker, New York, 1988.

[17] L.N. Phillips, Design with Advanced Composite Materials, Springer, London, 1989.

[18] R. Ramesh, Kishore, R.M.V.G.K. Rao, Dry Sliding Wear Studies in Glass Fiber Reinforced Epoxy Composites, Wear 89 (1983) 131.

[19] P.B. Mody, T.W. Chou, K. Friedrich, J. Mater. Sci. 23 (1988) 4319–4330.

[20] M. Sumer, H. Unal, A. Mimaroglu., Evaluation of tribological behaviour of PEEK and glass fibre reinforced PEEK composite under dry sliding and water lubricated conditions. Wear 265 (2008) 1061–1065.

[21] M.D. Lutton, T.A. Stolarski, The effect of water lubrication on polymer wear under rolling contact condition, J. Appl. Polym. Sci. 54 (1994) 771–782.

[22] D.C. Evans, Polymer fluid interaction in relation to wear, in: Proceeding of the third Leeds-Lyon Symposium on Tribology, The wear of Non-Metallic Materials, Mechanical Engineering Publication Ltd., 1978, pp. 47–55.

[23] J.K. Lancaster, Lubrication of carbon fiber-reinforced polymers. Part 1. Water and aqueous solution, Wear 20 (1972) 315–333.

[24] K. Tanaka, Friction and wear of semi crystalline polymers sliding against steel underwater lubrication, Trans. ASME J. Lubric. Technol. 102 (4) (1980) 526–533.

[25] H. Unal, A. Mimaroglu, Friction and wear characteristics of PEEK and its composites underwater lubrication, J. Reinforced Plast. Compos. 16 (2006) 1659–1667.

[26] C.J. Hooke, S.N. Kukureka, P. Liao, M. Rao, Y.K. Chen, The friction and wear of polymers in non-conformal contacts, Wear 200 (1996) 83–94.

[27] B. Suresha, G. Chandramohan, Siddaramaiah, P. Sampathkumaran, S.Seetharamu, Mater. Sci. Eng. A 443 (2007) 285–291.

Development of Magnisio Ferrite Doped Polymer Electrolyte System for Battery Application

Kamlesh Pandey* Markandey Singh, Nidhi Asthana, Mrigank Mauli Dwivedi, and S.L. Agrawal[1]
National centre of Experimental Mineralogy and Petrology, University of Allahabad, Allahabad-211002
[1]Department of Physics, A. P.S. University, Rewa (M.P.)
*kp542831@yahoo.com

Abstract-**Ion transport property of [93PEO-7NH_4SCN]: Mg-Zn Magnisio ferrite electrolyte system have been investigated here with the aim of developing a high performance solid state battery. Wet chemistry route has been adopted to obtain this electrolyte. XRD patterns (Debye-Scherer & Williamson Hall plot calculations) ascertain formation of nanocomposite system. Different ion transport parameters like bulk conductivity, dielectric loss, tangent loss and modulus spectra were studied with the aid of impedance spectroscopic data. Optimum d.c. conductivity has been observed for [93PEO-7NH_4SCN]: 1wt% Mg-Zn ferrite system ($9.0x10^{-5}$ S/cm) and a.c. conductivity of nanocomposite polymer electrolytes seems to follow the universal power law. Battery performance of this electrolyte was tested and OCV of best system is found to be 1.57 Volt.**

KeyWords-Dielectric Relaxation; Magnisio ferrite; Polymer nano composite; polymer salt interaction; PEO, Proton conducting battery.

I. INTRODUCTION

Nanocomposite polymer electrolyte (NCPE) materials are receiving special attention, particularly in the field of solid state ionics owing to their potential applications in advanced ionic devices such as high performance batteries, fuel cell, supercapacitor, sensors, smart window etc. [1-4]. NCPE have several distinct advantages over liquid electrolytes such as good mechanical properties, better thermal stability, corrosionlessness, light weight, flexibility and ease of fabrication / processibility as thin films etc. PEO is one of the most prominent polymer host which has been extremely investigated as polymer electrolyte using alkali salts, plasticizer and inorganic fillers in the recent past [5,6]. The other polymer host poly (vinyl alcohol) [PVA] , poly (vinyl chloride) [PVC], poly (vinylidenefluoride) [PVdF], poly (methyl methacrylate) [PMMA] have been also studied for potential material [7-12]. In spite of the industrial importance and wide application of PEO poly (ethylene oxide), the ions conduction mechanism remains unresolved. The chemical structure of PEO i.e. [$(CH_2\text{-}CH_2\text{-}0)_n$] explain most of the properties of this polymer, a strong solvating character due to high donating character of numerous either oxygen, strong tendency for crystallization correlated to high organization and rigidity of segmental units. As earlier most of workers have been stated experimental work, anion / cation mobility occurs in the amorphous phase and its diffusion occurs through a complex mechanism involving the PEO segmental mobility. For that, crystallization has to be avoided by modifying the pure polymer structure or by adding salt or by one or more plasticizer or filler to inhibit regular packing. Moderate conductivity in amorphous material is then a direct consequence of PEO features where high salvation is counter balanced by the energetic complexation of cations. Equilibrium between different solvated species (free ions, solvent separated ion pairs, ion pairs or high ions aggregation) also has a detrimental effect on cation mobility [13]. The addition of ferrite filler to PEO matrix enhances the polar characteristic of PEO making it electrically more conductive. When PEO is doped with ferrites, it may reside at various sites. It may go substitution on polymer chain at the amorphous or crystalline boundaries and preferentially into amorphous regions of polymer. Furthermore, it is asserted that addition of ferrite creates additional hopping sites for the charge carriers and hence increases in its concentration, increase the conductivity [14, 15].

In view of the above, an innovative approach has been made to use nanosized Mg-Zn ferrite ceramics material as filler in development of PEO-NH_4SCN electrolyte based NCPE and its electrical characterization in the present work. The structural aspect of composite electrolytes has been studied by XRD measurement and the effect of salt or filler in enhancement of a.c. conductivity of NCPE under different conditions. The frequency and temperature dependent behavior of dielectric, modulus spectra and a.c. conductivity have been investigated.

II. EXPERIMENTAL:

The Mg-Zn ferrite powder was synthesized by the standard sol-gel technique. Different nitrates were (like Mg (NO3)2.6H2O, Fe (NO3).9H2O and Zn (NO3)2.6H2O AR grade) have been used as the starting chemicals to obtain the Fe3+, Mg2+, Zn2+ & Fe2+ ions in aqueous solution. These nitrates were dissolved in double distilled water/ethanol mixture. The pH of solution was fixed within 2-3 range. The sol allowed to gel at 50oC. The gel was dried at 150oC for 20 h. Subsequently, this dried gel was subjected to thermal treatment at 700oC (for 2 hours) and 1000oC (for 2 hours) in kenthal high temperature furnace. The dried material was crushed to obtain fine powder of magnisio ferrite.

Composite polymer electrolyte films (~100-300µm thickness) were prepared using solution cast technique. The poly (ethylene oxide) PEO (mw~6x105 ACROS organics) and salt NH4SCN (Rankem India, AR grade) were used for the synthesis of composite electrolyte. The sol gel developed Mg-Zn ferrite powder was dispersed stoichiometrically in PEO-NH4SCN solution (in double distilled water at 40oC)

and stirred for 10-15 hours continuously. This gelatinous polymeric solution was finally cast in polypropylene dish. This solution cast film was dried at 30oC in B.O.D. incubator for controlled evaporation followed by vacuum drying to obtain the solvent free standing films of NCPE.

Structural behavior of Mg-Zn ferrite and PEO-NH4SCN: Mg-Zn ferrite system were studied by X-ray diffractometer (Phillips X-Pert model) in the Bragg's angle range (2θ) 15-60o using Cu-Kα radiation (λ=1.542 oA). Mossbauer study of magnisio ferrite powder was carried out by PC based spectrometer having 1024 channel MCA cord operating in constant acceleration mode. The SEM image of the different composite electrolyte system was recorded with JEOL JXA-8100 EPMA instrument. The electrical characterization of the solid polymer composite electrolyte was carried out using impedance spectroscopy on the application of small a.c. signal (~20mV) across the sample cell with Pt-blocking electrodes. The complex impedance parameter were measured with impedance analyzer (HIOKI LCR Hi-tester, model 3522, Japan) in the frequency range 40 Hz-100 KHz. Dielectric relaxation behaviors were carried out by the impedance data.

Solid State batteries are fabricated by sandwiching the solid electrolyte (NCPE in present studies) between two electrodes (cathode & anode). Hence the battery or cells consist of three major components i.e. anode, electrolyte and cathode. A typically, solid state cell in which NCPEs is sandwiched between anode and cathode of different chemical potentials μ1 and μ2 respectively. The solid state rechargeable batteries are assembled by two step process. In the first step, anode and cathode powdered materials are pressed in a pelletizing die to obtain pellets of electrodes. Since the focus of present work is to develop a proton conducting rechargeable all solid state battery, in order to supply protons, Zn+ZnSO4.7H2O with stoichiometric ratio 3:1 was chosen as anode material. The anode materials (Zn power & ZnSO4.7H2O) were crushed in agate to form fine powder. Thereafter this mixture was subjected to pelletizing die at ~5Kbar pressure for 20-30 minutes. Similarly cathode composite material comprising of (graphite, solid electrolyte, and any intercalation material like V2O5, MnO2, PbO2, and TiS2 in stoichiometric ratio 2:2:5) were again crushed and mixture was pelletized following the similar procedure. Finally, the NCPE sample possessing optimum conductivity were sandwiched between anode and cathode pellets. The cells dimension were approximately (dia-1.76cm, thickness 1to1.2cm and the so designed estimated cells weighed 2-4gram.

III. RESULTS AND DISCUSSIONS

A. Characterization of Mg-Zn Ferrite Powder:

X-ray diffraction pattern of sol gel derived magnesium zinc ferrite (magnisio ferrite) is shown in figure-1(a). The main reflections from the planes are identified as (220), (311), (400), (422) and (511) confirm to the earlier report on magnisio ferrite [16-19]. Appearance of prominent reflection from (311), (400) plane and absence of impurities peaks ascertain the formation of spinal cubic structure with single phase. From the XRD pattern for (311) plane lattice parameter was 0.85 a/nm obtained as which again tallies with reported data [JCPDS No. 00-008-0234] and thereby ascertain formation of mixed spinal magnesium-zinc ferrite. The relative concentration of Mg and Zn in ferrite structure is known to influence particle size and lattice parameter. The average particle size of the Magnisio ferrite powder was evaluated by the Scherer's formula and it is found to ~ 30 nm. Such a value suggests formation of nanoferrite.

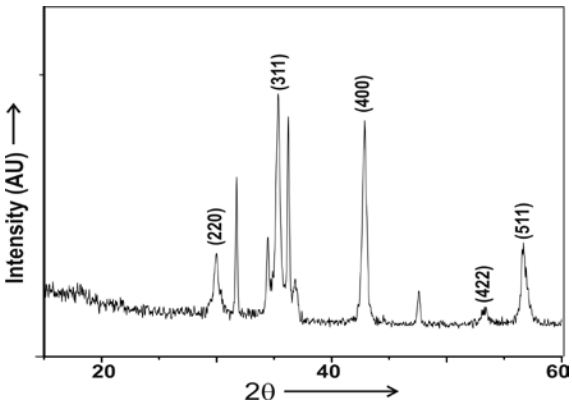

Figure 1 (a): XRD pattern of sol gel synthesized Mg-Zn ferrite powder.

RT.

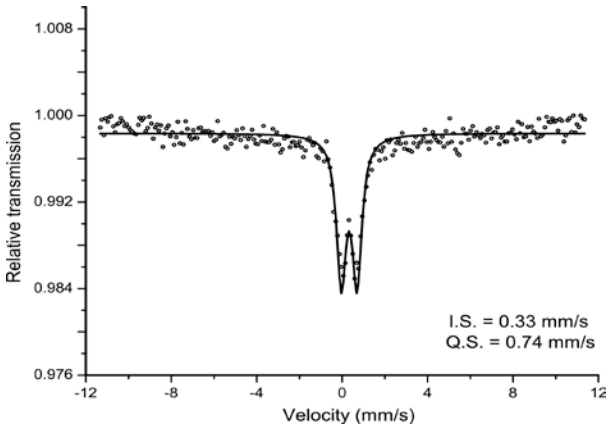

Figure 1 (b) Mossbauer Spectrum of nanosize Mg-Zn ferrite powder

Magnetic nano particle undergoing super paramagnetic relaxation is usually characterized by one of the powerful experimental technique namely, Mossbauer spectroscopy. At room temperature, in Mossbauer Spectrum the behavior of magnetic nano particles is quite interesting as they exhibit sextet (ferromagnetic state) and a doublet (super paramagnetic state). In Mossbauer Spectrum of Mg-Zn ferrite powder {shown in figure-1(b)} sample, the important observation is the appearance of a central doublet, related to absorption of quadrupole splitting. The spectra did not reveals any sextet. Careful examination of central doublet showed slight asymmetry to allow their assignment to presence of Fe3+ and Fe2+. The origin of central doublet components assigned to the Fe3+ ions and Fe2+ comes from super paramagnetic relaxation [20]. Further low value of isomer shift (IS~ 0.33mm/sec) and high value of quadrupole splitting (QS~ 0.74mm/sec) is attributed to small particle size (~nm) undergoing superparamagnetic relaxation at RT. Where, relaxation time τ is << τs (τs ~ characteristic time above blocking temperature). IS value of 0.33 mm/sec confirms only

the presence of Fe3+ was in ferrite sample while large Qs value indicates substantial electric field gradient around 57Fe nuclei due to small particle size.

B. Characterization of [93PEO-7NH4SCN]: x% Mg-Zn Ferrite Nanocomposite Polymer Electrolyte:

Structural behavior of [93PEO-7 NH4SCN]: x% Mg-Zn ferrite (where x= 0.5, 1, 2, 3, 4 and 5) system has been studied by XRD and SEM technique. The X-ray diffraction pattern of the different composite electrolyte system is shown in figure-2. In XRD pattern two main peaks at 19o and 23o (PEO characteristic peaks) with few other weak reflections are observed. Addition of salt and filler in polymeric host changes the intensity and broadness of existing original peaks. The increase in broadness or reduction in intensity is an indication of change (decrease) in crystallinity of pristine electrolyte. A comparative study of XRD peak at 23o shows splitting and broadening of the peak, with increase of filler content along with reduction in peak intensity. This reveals interaction of polymeric chain with salt and filler. The enlarged view of this interaction is also given in the inset of fig.-2 where we recorded few new peaks of Zn-Fe (2θ = 21.1o), Fe2O3 (2θ = 23.1o), Fe-Zn-CN (2θ = 23.3o), Zn (SCN)2 (2θ = 23.4o) and Fe-Zn(CN)6.2H2O (2θ = 23.5o). Existence of these peaks clearly supports interaction of PEO with NH4SCN and Magnisio ferrite. The average size of crystallites was calculated by the well known Scherer's formula [21].

$$t=0.9\lambda B\cos\theta \quad (1)$$

Where λ is the X-ray wavelength, θ the angle of Bragg's diffraction and B full width at half maximum (FWHM). The evaluated average crystallite sizes for different electrolytes were found to be 30-60 nm. In order to distinguish the effect of crystallite size induced broadening in FWHM of X-ray diffraction profile, Williamson-Hall (W-H) plot method [22] was adopted. In this method, crystallite size (without strain) is calculated from Sinθ vs. βCosθ plot {shown in figure-3} in accordance with the following relation.

$$\beta\cos\theta=C\lambda/t+2\varepsilon\sin\theta \quad (2)$$

Where C is the correction factor, ε the strain and λ, β and t have their usual meaning. The crystallite size (without strain) for different composite electrolyte system calculated by W-H plot method is given in table-1. These values ascertains nanometric dimension of synthesized electrolyte system.

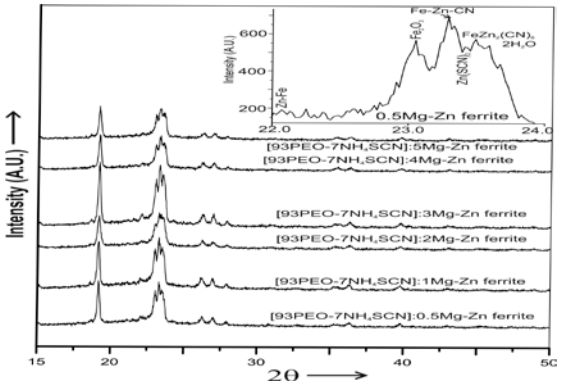

Figure 2: XRD pattern of (93 PEO-7NH4SCN): x% Mg-Zn ferrite film (where x = 0.5,1,2,3,4, 5). Enlarged view of the peak at 23° is given in inset.

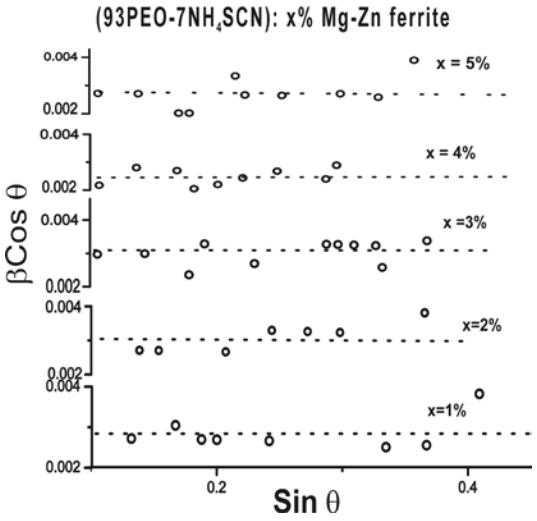

Figure 3: Williamson- Hall plots for different polymeric film.

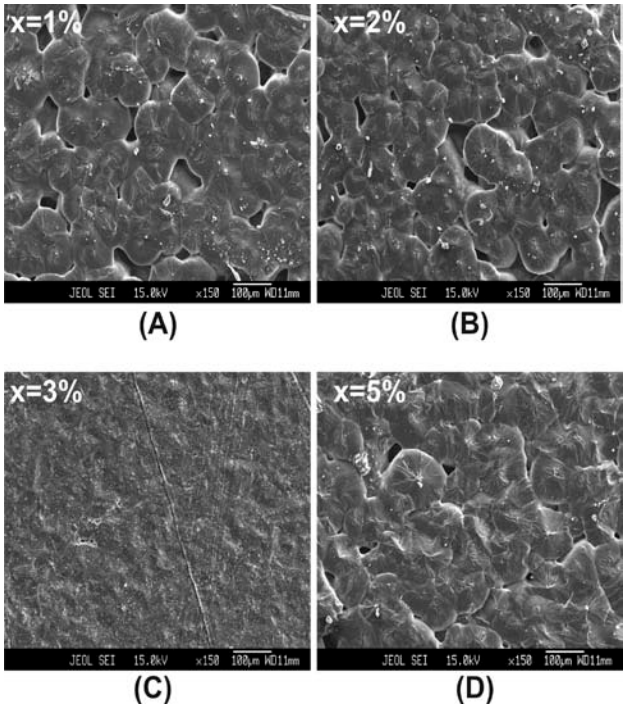

Figure 4: SEM image of (A) (93 PEO-7 NH4SCN):1% Mg-Zn ferrite film, (B) (93 PEO-7NH4SCN):2% Mg-Zn ferrite film, (C) (93 PEO-7 NH4SCN):3% Mg-Zn ferrite film and (D) (93 PEO-7 NH4SCN):5% Mg-Zn ferrite film.

SEM image of different compositions of [93PEO-7NH4SCN]: x% Mg-Zn ferrite (where x= 1, 2, 3 and 5 wt %) is given in figure-4. The images give the surface morphology and heterogeneous phase of nanocomposite electrolyte system. Pure PEO film has partial crystalline structure with formation of lamellar structure due to longer evaporation time used for drying the electrolyte films. Addition of Mg-Zn ferrite filler in [93PEO-7NH4SCN] electrolyte system make original entity looses this characteristic. Scanning electron images show that addition of filler disturbs the crystalline nature of original matrix. The particle size dimension during SEM analysis also supports the result of XRD studies.

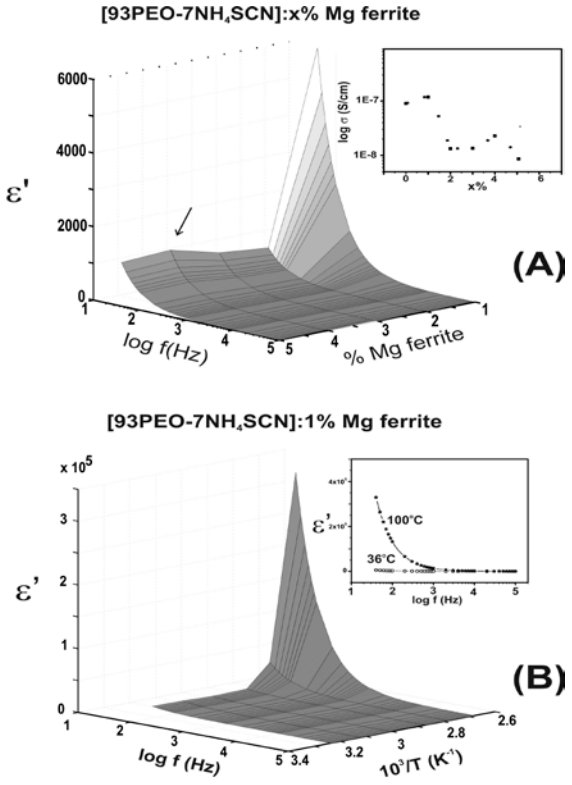

Figure 5 (a): Variation of Dielectric constant with frequency for different filler concentration (in inset Composition dependence of conductivity for polymer electrolyte system). (b): Variation of Dielectric constant with frequency and temperature for (93 PEO-7 NH4SCN):1% Mg-Zn ferrite film.

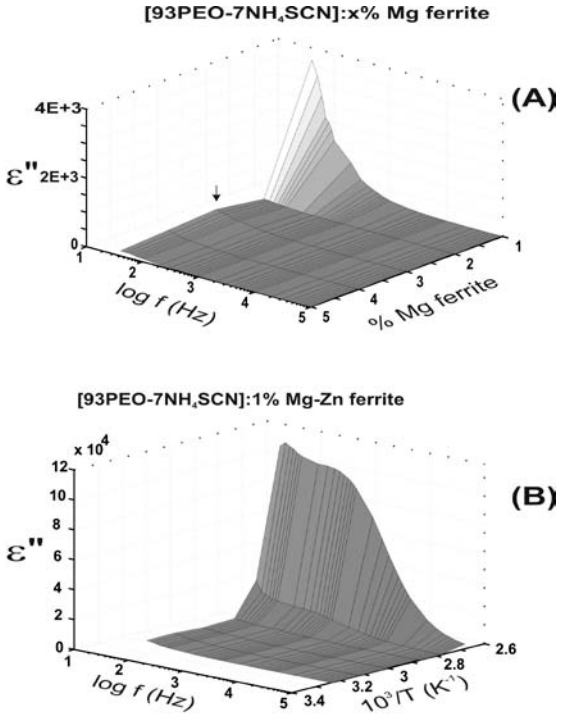

Figure 6 (a): Variation of imaginary part of Dielectric relaxation with frequency for different filler concentration. (b): Variation of imaginary part of Dielectric relaxation with frequency and temperature for){ 93 PEO-7 NH4SCN}:1% Mg-Zn ferrite film.

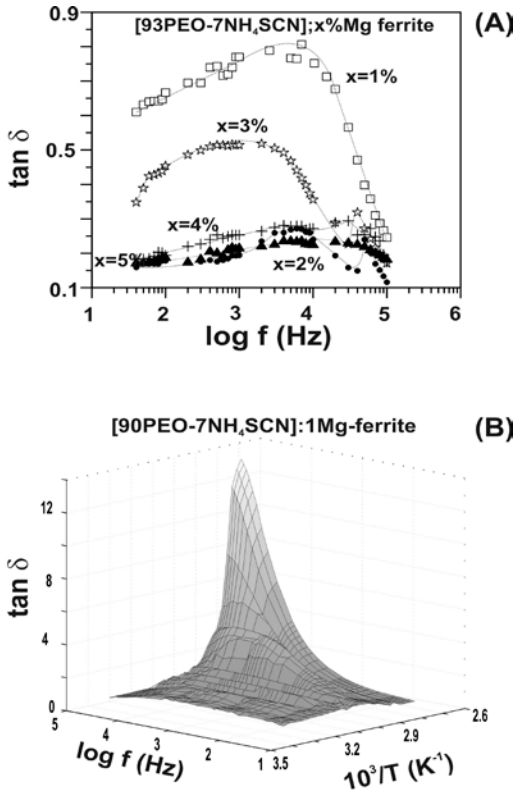

Figure 7 (a): Variation of Dielectric tangent loss with frequency for different filler concentration. (b): Variation of Dielectric tangent loss with frequency and temperature for {93 PEO-7 NH4SCN}:1% Mg-Zn ferrite film.

The change in relative dielectric constant of composite polymer electrolyte with frequency and Magnisio ferrite concentration is given in figure-5(a). Concentration dependence of ε′ shows two maxima: one at 1% Magnisio ferrite and the other at 4% magnisio ferrite concentration analogous to conductivity behavior. The change in bulk electrical conductivity with the ferrite composition is also given in the inset of figure-5(A) for comparison. Further strong frequency dispersion in relative permittivity (ε′) were recorded in low frequency region followed by a nearly frequency independent nature at higher frequencies above 10 KHz. Such a feature is typical of polymeric substance [23]. The decrease of ε′ with increasing frequency may be attributed to electrical relaxation or inability of dipoles to rotate rapidly leading to a lag between frequency of oscillating dipoles and that of applied field. As the frequency increases the ionic and orientational source of polarizibility decreases and finally disappears due to inertia of mobile ions which causes a constant value of dielectric constant [24]. This is possibly due to suppression of large scale heterogeneity in pristine complex and its replacements by small scale heterogeneity. The small scale heterogeneity is related to presence of Mg-Zn ferrite filler which increases the free volume on account of looser segmental packing of chain [25]. The frequency dependence of the dielectric constant on composition of electrolyte is explained as the polarizibility and potential movement of ions. In polymer host PEO, the oxygen ion is the mostly polarizable ion. Thus frequency dependent dielectric relaxation below 1 KHz could be related to ionic space charge carriers, such as oxygen vacancies, anti

site defects and interfacial polarization. Interaction of Mg-Zn ferrite with salt and polymer has been witnessed during XRD studied. This leads to formation of most easily polarizable non bridging oxygen. This enhances the dielectric constant of the composite system. The observed two maxima in dielectric constant can be associated to interfacial polarization followed by polarization resulting from polymer-salt- filler interaction. At high filler content i.e. beyond 1 wt% ferrite filler in electrolyte decrease the dielectric polarization comes from increase in crystalline behavior. A moderate rise in dielectric constant around 4 wt% filler content may be possibly due to the increase in polarizibility of polymer in the presence of ferrite. When the filler content is enhanced further its segregation takes place which reduces the polarizibility of composite system.

The variation of dielectric constant of [93PEO-7NH4SCN]: 1% Mg-Zn ferrite nanocomposite electrolyte system (maximum conductivity system) with frequency and temperature is given in figure 5(b). A strong dielectric dispersion was observed with increasing temperature. It is interesting to note that the non Debye nature of electrolyte system at low temperature and low frequency value was recorded while it continued to high temperature for higher frequency value. The observed behavior can be explained if the system is assumed to be formed of molecular dipoles. These dipoles remain frozen when the temperature is lower than (345oK). As the temperature increase beyond this critical temperature (Tc), the dipoles becomes more thermally activated having more rotational freedom, which leads to the observed increase in the dielectric relaxation.

The change in imaginary part of dielectric permittivity (or dielectric loss) with frequency and Mg-Zn ferrite concentration is shown in figure 6(a). The dielectric study gives two maxima for dielectric loss with variation of Mg-Zn ferrite content in consonance with dielectric constant variations. The value of ε″ is seen to decrease with increasing frequency at room temperature- a well known feature seen in polymer electrolytes [26]. Higher value of dielectric loss (ε″) at low frequency is due to the free charge motion within electrolyte. It also reflects the reorientation process of dipoles in polymer chain which gives a relaxation peak in dielectric loss spectra.

The Figure- 6(b) shows the variation of dielectric loss/ imaginary part of dielectric permittivity with frequency and temperature. The dielectric loss is noticed to increase with increasing temperature of [93PEO-7NH4SCN]: 1% Mg-Zn ferrite system. It is possibly due to formation of extra molecular dipoles in the system. These dipoles become thermally activated, having more rotational freedom. It is thus inferred that all types of polarization except for thermally activated space charge polarization may contributing to the dielectric polarization response in the low temperature range. On other hand, at higher temperature beyond melting temperature of polymer host, the thermally activated space charge may be contributing to polarization process, which leads to observed increase in ε″ and the dispersion process. The entire response reflects a non-Debye relaxation in composite electrolyte system.

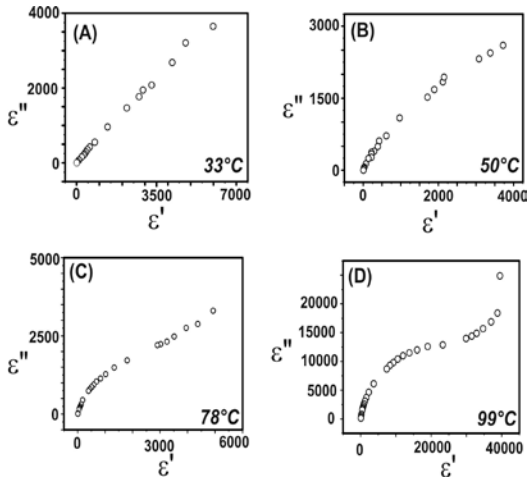

Figure 8 Cole- Cole plot for dielectric relaxation at different temperature for (93 PEO-7 NH4SCN):1% Mg-Zn ferrite film.

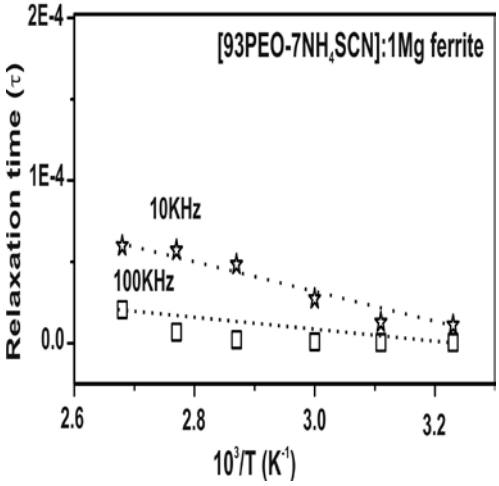

Figure 9 Variation of relaxation time with temperature for (93 PEO-7 NH4SCN):1% Mg-Zn ferrite film.

The frequency dependence of dielectric tangent loss (tanδ), at different compositions is shown in figure-7(a). The composition dependent curve of tangent loss shows a clear relaxation peak with increase in its broadness with the rise of Mg-Zn ferrite content, in composite system. And it was tend to decrease the peak frequency for relaxation. Also loss tangent value decreases significantly with increasing ferrite concentration (up to 2wt %) and thereafter it increases, before finally decreasing due to segregation of filler in polymer chain. This nature is also a reflection of two peaks characteristics of the system. The loss peak can be successfully explained in term of the dielectric relaxation process associated with the presence of crystal heterogeneity in the polymer electrolyte matrix [27]. All these results show that enhancement of Mg-Zn ferrite content tend to looses the segmental packing in the chain thereby increasing the free volume for dipolar relaxation. XRD studies shows that addition of filler enhances the amorphousity of the polymer electrolyte film up to a certain limit. This peak can be attributed to segmental diffusion motion in amorphous region and assignable to β (beta) relaxation process.

TABLE-1: AVERAGE PARTICLE SIZE FOR DIFFERENT POLYMER COMPOSITE ELECTROLYTES.

S No Sample	particle size by Scherer's formula(nm)	particle size by W.H Plot(nm)
1. $Mg_{1-x}Zn_xFe_2O_3$(Magn is io ferrite)	29.5	22.5
2. [93PEO-7NH $_4$SCN]:0.5% Mg -Zn ferrite	47.2	43.5
3 . [93PEO-7NH $_4$SCN]:1% Mg -Zn ferrite	45.8	31.0
4 . [93PEO-7NH $_4$SCN]:2% Mg -Zn	38	35
5 . [93PEO-7NH $_4$SCN]:3% Mg -Zn	57	45
6 . [93PEO-7NH $_4$SCN]:4% Mg –Zn	35	32
7 . [93PEO-7NH $_4$SCN]:5% Mg -Zn ferrite	59	52

The variation of tangent loss with frequency and temperature is shown in figure -7(b). From the curve it can be noted that, as the frequency increases the peak maxima tend to shift to higher temperature, indicating the temperature dependence of the relaxation time. Presence of relaxation dipoles may be due to the orientation of the polar groups present in the side group of the polymer. This type of relaxation is called the dipolar group relaxation.

The dielectric behavior for the polymeric material can be described by the Cole-Cole expression [28, 29].

$$\varepsilon^* = \varepsilon_\infty + \Delta\varepsilon(1+i\omega\tau)^y \quad (3)$$

Where ε∗ is complex dielectric constant, Δε= ε–ε∞ the static dielectric constant, ε∞ the relative dielectric constant at very high frequency, τ the effective relaxation time, y a parameter (defined as angle of semicircular arc) where value lies in the range 0< y<1 to describe the distribution of relaxation time and ω= 2πf is the angular frequency. When y =1 the equation gives semicircle (cole-cole plot) in the plot of ε″ verses ε′ and reduced to the non cooperative single relaxation following in the linear Arrhenius relation [30]. The variation of ε″ (imaginary part) versus ε′ (real part) i.e. cole-cole plot is shown in figure-8. In the Cole-Cole plot the decrease in diameter of semicircle is observed with increase in temperature.

Based on equation (3), the relaxation frequency of dielectric absorption f max is expressed as

$$2\pi f_{max} = \tau \quad (4)$$

Where the dispersion and absorption curves are symmetrical about the position ωτ = 1. The relaxation time τ is determined by experimentally obtained frequency fmax. The calculated relaxation time for this system is ~ 8.5x10-5 sec. Figure-9 shows the variation of relaxation time (τ) against reciprocal of absolute temperature. The relaxation time linearly increases with temperature. This gives Arrhenious type thermally activated process. The slope yield activation energy for dielectric relaxation process.

For the study of electrode polarization/interfacial polarization effect in the nanocomposite electrolyte system as mentioned earlier the dielectric spectra and its scaling by complex modulus electric spectra was carried out [31].

The complex modulus can be evaluated from the following relation

$$M = M' - j\,M''$$

$$M' = \varepsilon''/\{(\varepsilon'')^2+(\varepsilon')^2\} \text{ and } M'' = \varepsilon'/\{(\varepsilon'')^2+(\varepsilon')^2\} \quad (5)$$

Figure -10 shows the real and imaginary part of dielectric modulus with frequency at different temperature (36-100oC) for [93PEO-7NH4SCN]: 1% Mg-Zn ferrite nanocomposite electrolyte system. The real part of modulus spectra increases with increasing frequency and decreases with increasing temperature. Also the imaginary part of dielectric modulus spectra increases with increasing temperature and frequency. In this case, electrode polarization / interfacial polarization effect is seen to completely vanish in contrast to the dielectric formalism. This is observed around frequencies (<500Hz). The appearance of peak in imaginary part of the dielectric modulus can be assumed to be related with the translation ionic dynamics and the conductivity relaxation of the mobile ions. We have also examined the scaling behaviour of the modulus function. M' and M" spectra scaled by M"max and frequency axis scaled by the relaxation frequency f max are shown in figure -10(b) and (d) for [93PEO-7NH4SCN]: 1% Mg-Zn ferrite nanocomposite electrolyte system.

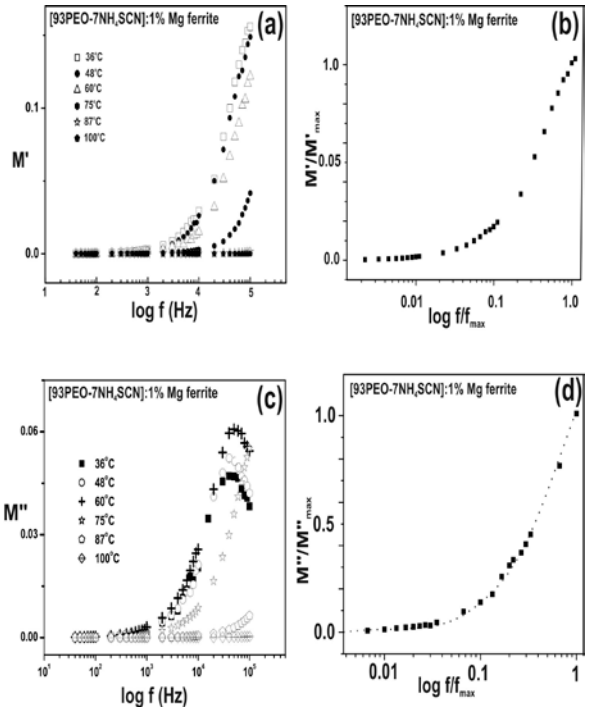

Figure 10: Variation of (a) Real part of electric modulus (M') with frequency at different temperature (b) Normalize M' with normalize frequency (c) Imaginary part of electric modulus (M") with frequency at different temperature and (d) Normalize M" with normalize frequency.

The variation of a. c. conductivity with different filler concentration in [93PEO-7NH4SCN]: x% Mg-Zn ferrite nanocomposite electrolytes system are given in figure- 11(a). The a. c. conductivity of 1% Mg-Zn ferrite filler content remains same with increasing the frequency, but for higher ratio of ferrite a. c. conductivity decreases with ferrite content. For other compositions i.e. for [93PEO-7NH4SCN]: x% Mg-Zn ferrite (x= 2, 3, 4, & 5%), the conductivity increases monotonically with frequency and beyond 10 KHz it rapidly grows (to form a peak). The frequency dependent conductivity in solid polymer electrolyte system seems to follow Universal power law [32].

TABLE-2 BATTERIES PARAMETERS OF NANO COMPOSITE POLYMER ELECTROLYTES

Solid State rechargeable battery parameters	OCV (Volt)	Current (I) (μA)	Electric Power (P) (μW)	Electric energy (E) (μWh)	Current density (J) (μAcm^{-2})	Power density (μW/Kg)	Energy density (μWh/Kg)
[93PEO-7NH_4SCN]:1% Mg-Zn ferrite	1.57	1.4	1.69	2.53	0.71	670	1003

$$\sigma_{ac}=\sigma_o+A\omega^n \quad (6)$$

Where, σo is the dc conductivity (extrapolation of the platue region to zero frequency gives the d. c. ionic conductivity), A the pre-exponential factor and n the fraction exponent laying between 0&1. The calculated value of conductivity for the best conducting electrolyte i.e. [93PEO-7NH4SCN]: 1% Mg-Zn ferrite composition is σo = 9.0x10-5 S/cm, and n=1. The change in a. c. conductivity is not prominently observed with applied frequency. This means that the charge carriers are not sufficiently free to follow the changing electric field and therefore conductivity remains nearly frequency independent. Figure -11(b) shows the variation of a. c. conductivity against frequency and temperature for [93PEO-7NH4SCN]: 1% Mg-Zn ferrite. In NCPEs a.c., conductivity increases linearly with frequency and temperature.

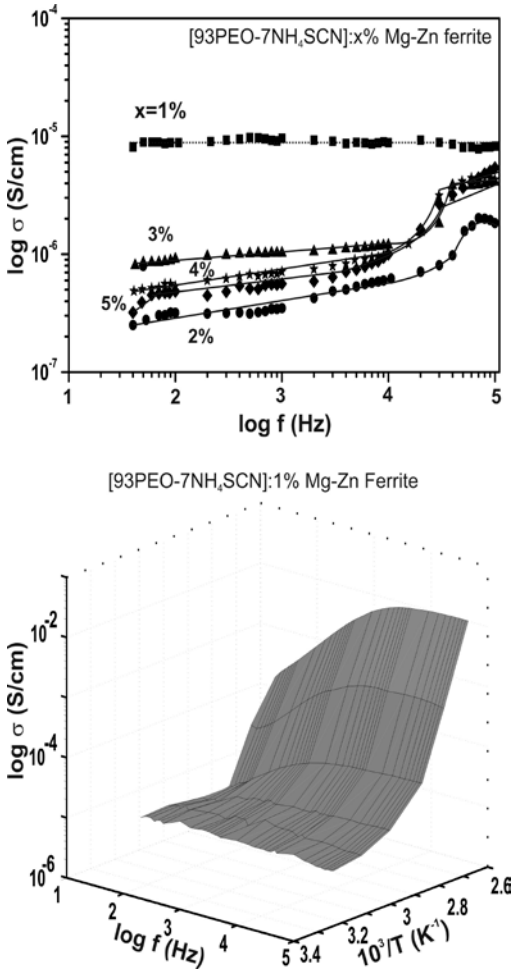

Figure 11 (a): Variation of ac conductivity with frequency for different composition of nano polymer composite electrolytes at ambient temperature. (b):Variation of ac conductivity with frequency for [93PEO-7 NH4SCN]: 1% Mg-Zn ferrite at different temperature.

In order to study the physical mechanism of the induced dielectric constant, the frequency dependence of the dielectric constant (ε'), imaginary part of dielectric permittivity (ε″) and a.c. conductivity at room temperature were plotted as figure-12. Dielectric constant (ε') exhibits asymptotic drop with increasing frequency. Further the slope of ε″ vs. frequency is found to be near (-1) in low frequency range. The dielectric loss tanδ (as given in fig-8) mainly consists of two contributions one from the dielectric polarization process $\tan\delta_{relax.}$ and other from d.c. conduction $\tan\delta_{dc}$. So $\tan\delta_{ac}$ can be expressed as,

$$\tan\delta_{ac}=\sigma_{dc}\omega\varepsilon \quad (7)$$

Where $\omega = 2\pi f$ equation (7) can be rewritten as $\varepsilon''_{dc}= \sigma_{dc}/\omega$. This means that the slope of log ε''_{dc} vs log ω (or log f) is -1. This slope (-1) indicates that the predominant dc contribution in the studied nanocomposite polymer electrolyte system [33, 34].

Once of the basic requirements of these entire polymer electrolytes is high ionic conductivity over a wide temperature window to establish their worth in electrochemical devices. Thus, besides structural, thermal and electrochemical characterizations, electrical characterization of NCPE is yet another important factor. Keeping this in mind electrical characterization on the developed nanocomposite polymer electrolytes was pursued.

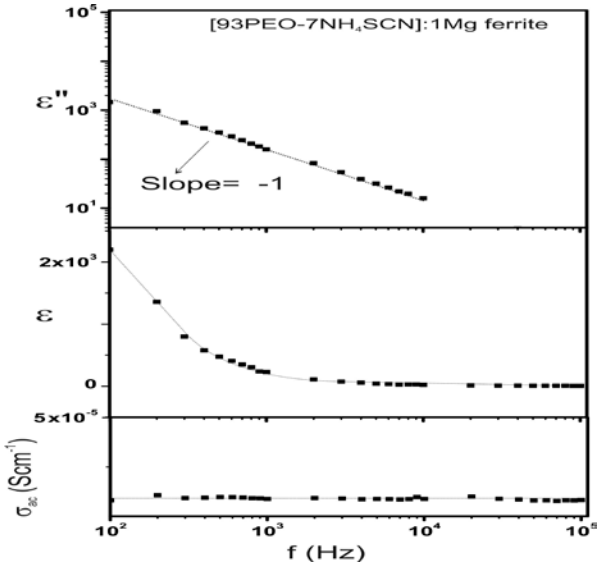

Figure 12: Frequency dependence of the ε', ε" and ac conductivity for[93PEO-7NH4SCN]: 1% Mg-Zn ferrite system.

The performance of a battery is evaluated from the cell parameters [35-37]. Various related parameters on the batteries based on NCPE were estimated. The open circuit voltage (OCV) of fabricated were noted using high resolution multimeter and were found to be 1.57 V of Mg-Zn ferrite

doped NCPE for [93PEO-7NH_4SCN]: 1% Mg-Zn ferrite. After OCV measurements these cells were subjected to self discharge without any application of load for long time and these cells were charged again on the application with constant current and 3V potential. The charge discharge characteristics were recorded on different load conditions. These parameters were calculated using following relations [38].

1) Electric Power (P):

This is the product of cell voltage (V) and current (I) delivered to the external load of resistance (R)

$$P = V.I = I^2R = V^2/R \text{ [W]}$$

2) Electric Energy (E):

This is the product of power and the discharge time in hour

$$E = V.I.t = q.V \text{ [Wh]}$$

3) Energy Density (Volume Capacity):

This is defined as the ratio of electric energy (E) and battery volume (v) in

$$E.D. = E/v \text{ [Wh/cc]}$$

4) Specific Energy (Weight Capacity):

This is the ratio of electric energy (E) and battery weight (m)

$$S.E. = E/m \text{ [Wh/Kg]}$$

5) Specific Power (Power Density):

This is defined as the ratio of electric power (P) and battery weight (m) in

$$P.D. = P/m \text{ [W/Kg]}$$

6) Current Density (J)

It is the defined as of current (I) and area of the cell

$$J = I/A \text{ [A/cm}^2\text{]}$$

All the fabricated cells were found to run for more than 200h at low current drain (1.5μA/cm^2). Further, the cell can withstand 10-20 cycles making it suitable low current density applications. All these parameters were determined in the plateau region of the cell potential discharge profile by 1MΩ resistance and values have been listed in table-2.

IV. CONCLUSIONS

The experimental studies through XRD, SEM, dielectric relaxation and electrical conductivity show that the Mg-Zn ferrite nano-filler changes the physical and morphological behavior of nano-composite electrolyte. Mossbauer investigations reveal the superparamagnetic nature of the Magnisio ferrite powder. XRD and SEM observations confirm formation of nano-composite system with crystallite size varying in between 30-60 nm. The electrical conductivity is enhanced by ~3-4 orders upon dispersion of ferrite and which also controls the gap of crystalline and amorphous conductivity. OCV of proton conducting battery were found to be 1.57 Volt.

ACKNOWLEDGMENT:

Thanks to BRNS, Dept. of Atomic energy Govt. of India for the financial support (No. 2009/34/25/BNRS) for this work.

REFERENCES

[1] Owen J. R , Superionic solids and solid electrolytes recent trends, 1989, In: Laskar A.L., Chandra S. ed. Academic Press, 111.

[2] Agrawal R. C., Pandey G. P. 2008 J Phys. D: App. Phys.41 223001.

[3] Koo J.H., Polymer nanocomposites: processing, characterization, andapplications, 2006 McGraw-Hill Professional 79.

[4] Pandey K., Dwivedi M. M., Tripathi M., Singh M. and Agrawal S.L 2008 Ionics 14 515.

[5] Maccallum J. R., Vincent C.A. 1987 Polymer Electrolyte Reviews, Elsevier. Applied Science.

[6] Chandra A., Srivastava P. C., Chandra S. 1995 J. Mater. Sci. 30 3633.

[7] Awadhia A., Patel, S.K., Agrawal S.L. 2006 Progress in Crystal Growth and Characterization of Materials 52 61.

[8] Alamgir, M., Abraham, K.M. 1993 J .Electrochem. Soc. 140 L96.

[9] Rajendran S., Uma T., 2000 Mater. Lett. 44 208.

[10] Tsuchida H., Toko T., 1983 Jpn. J. Appl. Phys. 22 1543.

[11] Bohnke O. and Vuillemin B., 1992 Mater. Sci. Eng. B 12 243.

[12] Appetechi G.B., Croce F., Scrosati B., 1995 Electrochim. Acta 40 991.

[13] Tanwar A., Gupta K.K., Singh J.P., Vijai Y.K., 2006 Bull. Mater. Sci. 29 397

[14] Pandey K., Dwivedi M. M., Singh M., Agrawal S. L., 2010 Journal of Polymer Research, 17 127.

[15] Iyer R., Desai R. Upadhyay R.V., 2009 Bull. Mater. Sci. 32 141.

[16] Rittidech A., Porkornwong N., Suthapintu A., 2009 Ferroelectrics, 382 62.

[17] Bharathi Kannan R., Chandramohan A., Chandra Sekar J., Kandhaswamy M. A., 2007 Crystal Research and Technology, 42 595.

[18] Mazen S.A., Mansour S.F., Zaki H.M., 2003 Cryst. Res. Technol., 38 471.

[19] Bammannavar B.K., Naik L.R., Pujar R.B., Chougule B.K., 2007 Indian J. Engg. & Mater. Sci. 14 381.

[20] Nath B.K., Chakrabarti P.K., Das S., Kumar U., Mukhopadhyay P.K., Das D. 2005 J. Surface Sci. Technol., 21 169.

[21] Cullity B.D. 1978 Element of X-ray diffractinon, Anderson-Wesley, 2nd ed. 281

[22] Williamson G.K., Hall W.H. 1953 Acta Metall. 1 22.

[23] León C., Lucía M. L., Santamaría 1997 J., Physical Review B 55 882.

[24] Pradhan D.K., Choudhary R.N.P., Samantaray B.K. 2008 Int.J. Electrochem.Sci., 3 597.

[25] Waser R., Baiatu T., Hardtl K.-H., dc electrical degradation of perovskite-type titanates: I ceramics, 1990 J. Amer. Ceram. Soc.73 1645.

[26] Pandey K., Dwivedi M. M., Das I.M.L., Singh M., Agrawal S. L. 2010 Journal of Electroceramics, 25 99.

[27] Marzantowicz M., Dygas J. R., Krok F., Florjanczyk Z., Zygadlo-Monikowska E., 2006 J. Non-Crystalline Solids, 352 5216.

[28] Kundu R.S., Bhatia K.L., Kishor N., Jain V. 1996 Philos. Mag.B. 74 317.

[29] Chaudhari B.K., Chaudhari K., Som K.K., 1989 J. Phys. Chem. Solid, 50 1149.

[30] Blythe A.R.1977 Electrical Properties of Polymers, Cambridge University Press.

[31] Moynihan C.T., Boesch L.P. Laberge N.L.1973 Phys. Chem. Glasses 14 122.

[32] Jonscher A.K. 1983 Dielectric Relaxation in Solids, London: Chelsea Dielectric Press.

[33] Chen A., Zhi Y. 2000 Phys. Rev. B 61 11363.

[34] Chen A., Zhi Y., Cross L.E., Guo R., Bhalla S.A. 2001 Appl. Phys. Lett. 79 818.

[35] Scheers J., Johansson P., Szczecinski P., Wieczorek W.,Armand M., Jacobsson P., Scheers J., Johansson P., 2010 Journal of Power Sources 195 6081.

[36] Syzdeka J., Armand Michel, Gizowskaa M., Marcinek M., Sasima E., Szafran M., Wieczorek W. 2009 Journal of Power Sources 194 66.

[37] Pandey K., Laksmi N., Chanrda S. 1998 Journal of Power Sources 76 116.

[38] Julien C., Nazri G.A.1994.Solid State Batteries: materials Design and Optimization, Kluwer Academic Publishers, London,

Study on Preparation of Composite Materials of Montmorillonite

Fu Guizhen，Liu Hong，Gong Wenqi
School of Resources and Environmental Engineering,
Wuhan University of Technology, Wuhan ,China
fgzh@163.com

Abstract- **Granulated composite materials were prepared by using the mixture of montmorillonite, fly ash and certain amount of cementing agent. The granulated composite materials were used to treat waste water containing Cu^{2+}. The mixture ratio of montmorillonite/fly ash, temperature of calcination and the amount of cementing agent were investigated. The experimental study results showed that the optimum technological conditions of preparing composite materials were as follows: the mixture ratio of montmorillonite and fly ash was 6:4; the calcination temperature was 450°C; the proportion of industrial starch used as an additive was 10%; the diameter of the granular was 1～2mm. Physical tests of granulated adsorption materials showed that the water adsorption capacity was 31.80%, the apparent porosity was 46.82%, the bulk density was 1.47 kg/m^3, the compressive strength was 5.28 MPa, and the surface area was 10.28 m^2 / g. The composite adsorbent materials prepared under the above conditions exhibited high adsorptive performance.**

Keywords-montmorillonite; fly ash; granulation; adsorption

Montmorillonite has been studied with great progress in the application of environmental protection since 1980s. Montmorillonite was used as environmental protection material primarily in wastewater treatment, which could be seen from the present references. Whether montmorillonite as single sodium modified or composite materials, the main purpose is to improve its adsorption capacity to use as adsorbent in wastewater purification. It not only absorbs a mass of organic suspended matter and heavy metal irons, but also removes microorganism such as bacteria, virus and other microorganism. Therefore, the montmorillonite and its products can be used for treating a variety of wastewater. Furthermore, lots of researches indicated that utilizing montmorillonite to treat wastewater contained heavy metal irons showed not only better effect but also much more economical, which explored a feasible way for the exploitation and utilization of montmorillonite.

It was attracted much attention that using montmorillonite mineral, fly ash and other industrial wastes as adsorption materials to remove heavy metal irons in wastewater because of its obvious economic benefits and social significance. Most of the treatment technologies adopted powdery adsorbent to process wastewater，but it was very difficult for the subsequent solid-liquid separation process，because the powdery adsorbent material was very small and easy to disperse when it was mixed with water. It was easy to form new industrial sludge which would have much more harmfulness of secondary pollution due to the concentration of heavy metal irons. Although the treatment effect of powdery adsorbent was fine, it had many problems in practical application. In order to solve the above problems of powdery adsorbent processing wastewater the experiment was made to study the technological conditions of preparing the granulated adsorption materials of montmorillonite and its adsorption performance on Cu^{2+}.

I. EXPERIMENTAL

A. Materials

The raw materials used in the experiments were the calcium montmorillonite from Liaoning province and the fly ash from a coal-fired power plant in Wuhan. The X-ray fluorescence spectrometer quantitative analysis was made by Test Center of Wuhan University of technology. The chemical composition of montmorillonite and fly ash was as Table 1 and Table 2.

TableI CHEMICAL COMPOSITION OF MONTMORILLONITE

Ingredient	SiO_2	Fe_2O_3	Al_2O_3	TiO_2	CaO	MgO	K_2O	Na_2O
Wt%	56.78	6.56	17.03	0.73	2.76	3.65	0.85	0.39

Ingredient	MnO	H_2O^+	H_2O^-	ignition loss	total
Wt%	0.08	10.29	4.23	10.04	99.46

TableII CHEMICAL COMPOSITION OF FLY ASH

Ingredient	SiO_2	Al_2O_3	Fe_2O_3	TiO_2	CaO	MgO	K_2O	Na_2O
Wt%	38.66	20.86	4.25	0.98	18.94	1.21	1.81	0.42
Ingredient	SO_3	P_2O_5	Ignition loss	Total				
Wt%	3.33	0.35	8.64	99.45				

B. Instruments and reagents

The instruments and reagents used in the experiments were shown as Table 3 and Table 4.

TableIII EXPERIMENTAL INSTRUMENT LIST

Equipment	Type	Manufacturer	Use
Air-bath oscillator	HZQ-C	Harbin Donglian Electronic &Technology Development Co., Ltd	Oscillation adsorption
Electric-heated thermostatic air-blowing dryer	DHG－9075A	Shanghai Yiheng Instruments Company	Dry
Resistance furnace temperature controller	KSY-12-16S	Shanghai Experimental Electric Furnace Factory	Roasting
High speed tabletop centrifuge	800	Shanghai Surgical Instrument Factory	Solid-liquid separation
Flame atomic absorption spectrometer	AVANTA M	Australia GBC Company	Ion concentration determination
Specific surface area and aperture tester	2360	American Gemini Company	Specific surface area determination
X-ray diffraction	D/MAX-IIIA Axios	Japan RIGAKU Company	Phase analysis
X-ray fluorescence spectrometer Transmission electron microscopy	H-600STEM/EDX PV9100	The Dutch Panalytical Company Japan HITACHI Company	Quantitative analysis Morphology analysis

TableIV EXPERIMENTAL REAGENT LIST

Drug	Chemical formula	Purity	Manufacturers
Copper sulfate	$CuSO_4{\cdot}5H_2O$	Analytically pure	Tianjin Bodi Chemical Co., Ltd
Sodium acetate anhydrous	$C_2H_3NaO_2$	Analytically pure	Sinopharm Chemical Reagent Co., LtdS
Glacial acetic acid	CH_3COOH	Analytically pure	Tianjin Guangcheng Chemicals Co., Ltd
Sodium ethylene diamine tetraacetate	$C_{31}H_{28}N_2Na_4O_{13}S$	Analytically pure	Tianjin Guangcheng Chemicals Co., Ltd

C. Methods

1) Preparation of Montmorillonite Composite Particle Materials:

The montmorillonite composite particle materials were prepared using appropriate amount of montmorillonite and fly-ash, mixing with a certain proportion of additives, adding appropriate amount of distilled water and standing aging, making by hand to form spheric particles with the diameter of 1～3mm, natural aging for 40min and then drying for 1h under 105℃ , finally roasting at high temperature for 2h.

2) Method for Adsorption Experiments:

A certain quantity of standard Cu^{2+} solution and

amount of montmorillonite composite particles adsorbent were added into volumetric flask, mixing adsorbed in an oscillator, centrifugalized with a high speed tabletop centrifuge. 5mL centrifugal solution, 5mL buffer solution and 5mL 0.1mol/L EDTA were added into a 50mL tube. Then distilled water was added to 50mL scale line and shaken well. The absorbency of solution was determined by a grating spectrophotometer of 7200 type under the wavelength of 733nm and compared with that there was not added Cu^{2+} solution. The concentration of Cu^{2+} solution was calculated. The adsorption efficiency of Cu^{2+} on montmorillonite/fly ash composite materials was calculated according to the concentration changes before and after adsorption.

Adsorption ratio was calculated as follow formula:

$\eta=(Co-C)\times100\%/Co$

η: adsorption ratio of Cu^{2+} on composite particles adsorbent (%)

Co: concentration of Cu^{2+}before adsorption (mg/L)

C: concentration of Cu^{2+}after adsorption (mg/L)

3) Determination of Granular Spallation Lost Ratio:

A certain amount of particles were taken into conical flask with 100mL distilled water and oscillated in a stable temperature horizontal shaking bath with the frequency of 110r/min for a while at a certain temperature. Then the powder produced by crushing adsorption material was washed by deionized water and rest wet granules were dried up to constant weight in the drying oven. The quality of remaining intact granules was weighed after cooling down to room temperature.

Granular spallation lost ratio was calculated as the following formula:

$q=(Mo-M)\times100\%/Mo$

q: granular spallation lost ratio(%)

Mo: quality of granules before adsorption (g)

M: quality of remaining intact granules after adsorption (g)

II. STUDY ON THE PREPARATION TECHNOLOGY OF GRANULATED COMPOSITE ADSORPTION MATERIALS OF MONTMORILLONITE

The results of preparation technology research of granular adsorbent showed that adsorption ratio and spallation lost ratio of granules were influenced by several factors, which were calcination temperature, ash rate, proportion of additive, particle size of adsorbent and calcinations time. The purpose of this experiment was to prepare adsorption materials with both high adsorption ability and suitable strength, but it seems always contradictive. Therefore, the two factors would be comprehensively considered in this experiment in order to determine the optimum technological conditions.

A. Effect of Calcination Temperature

A certain quantity of montmorillonite and fly ash were weighed and mixed by the ratio of 5:5, and some additives were added into the mixture. Montmorillonite/ fly ash composite particles were prepared as above technology. They were roasted for 2h under different temperature conditions in muffle furnace, and cooled down to the room-temperature. The composite particles were used to process simulated wastewater contained Cu^{2+}. Adsorption experimental conditions were as follows: the initial concentration was 200 mg/L; the adsorbent of granules was 12g/L; the adsorption reaction time was 60min. Experimental results were shown in Fig.1.

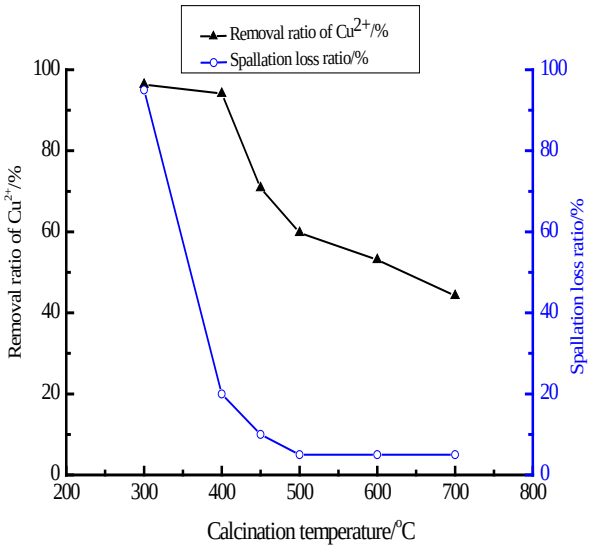

Fig.1 Effect of calcination temperature on removal efficiency

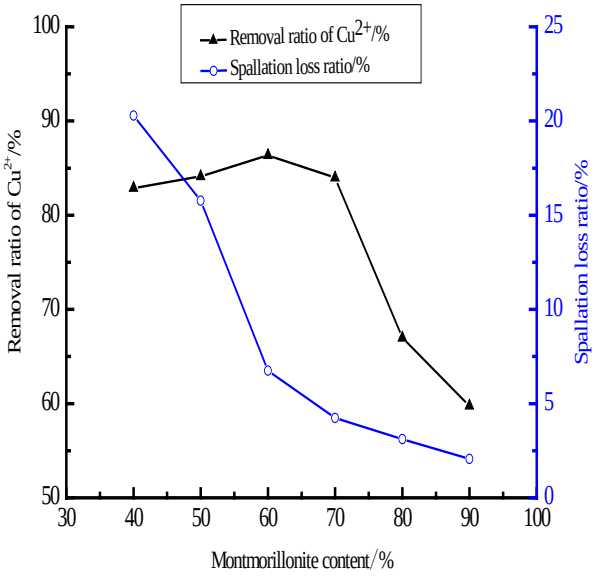

Fig.2 Effect of mixing ratio of montmorillonite and fly ash on removal efficiency

Fig.1 showed that both the curves of removal rate of adsorption and lost ratio were downtrend with the increase of calcination temperature. When the temperature was 300℃, there was the highest adsorption rate of 96.34％ and spallation lost ratio of 95％. When the temperature was 700℃, adsorption rate and lost ratios was 5％and 44.23％respectively. Therefore, high temperature calcination was in favor of increasing particle strength, but it decreased the adsorption

rate correspondingly. High strength and high adsorption rate could not be given consideration simultaneously. When the temperature was 450℃, adsorption rate was 70.84% and lost ratio was10％. Calcination temperature was determined as 450℃ after comprehensively considering, so the calcination temperature of subsequent experiments was fixed at 450℃.

B. Effect of Mixing Ratio of Montmorillonite/Fly Ash

A certain quantity of montmorillonite was weighed and mixed with fly ash by different mass ratios. Composite particles of montmorillonite/ fly ash were prepared and the calcination temperature was 450℃. An adsorption experiment was made after the granules cooled down to room-temperature under the same conditions of 2.1. Experimental results were shown in Fig.2.

Fig.2 showed that removal rate of adsorption was downtrend while spallation loss ratio decreases sharply with the increase of content of montmorillonite. When montmorillonite content was 40-60％, adsorption rate of granular adsorbent was higher as well as spallation loss ratio. When montmorillonite content was more than 60％, loss ratio had not changed much more but adsorption rate decreases sharply. Thus, montmorillonite content was determined on 60％: The best mixture ratio of montmorillonite and fly ash was 6:4. So mixture ratio of montmorillonite and fly ash of subsequent experiment was fixed on 6:4.

C. Effect of Additive Ratio

A certain quantity of montmorillonite and fly ash were weighed and mixed by the ratio of 6:4. Industrial starch was added with different mass ratios. Composite particles of montmorillonite/ fly ash were prepared by the technology of 1.3.1 and calcination temperature was 450℃. Adsorption experiment was carried after the granules cooled down to room-temperature under the same conditions of 2.1. Experimental results were shown in Fig.3.

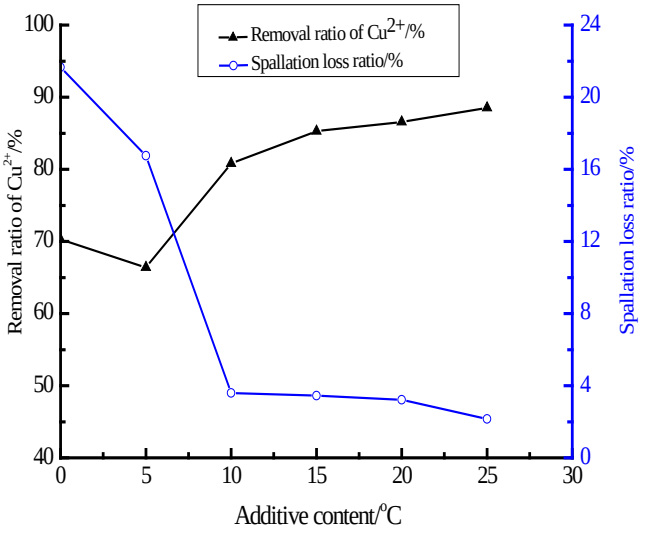

Fig.3 Effect of additive ratio on removal efficiency

Fig.3 showed that adding a few industrial starches could play a role of bonding and decrease granular spallation loss ratio. But bonding effect was unconspicuous and mainly played a role of foaming agent when the additive ratio exceeded 10%. Roasted starch could increase the pore of granular adsorbent with the result that increased the removal rate of adsorption. The additive ratio was determined as 10% of the mixture quality.

D. Effect of Granulated Diameter

A certain quantity of montmorillonite and fly ash were weighed and mixed by the ratio of 6:4. Industrial starch was 10% of the quality of mixture. Granular adsorbents of different diameters were prepared by the technology of 1.3.1 and calcination temperature was 450℃. Adsorption experiment was started after the granules cooled down to room-temperature，and other conditions were as same as 2.1. The results were shown in Fig.4.

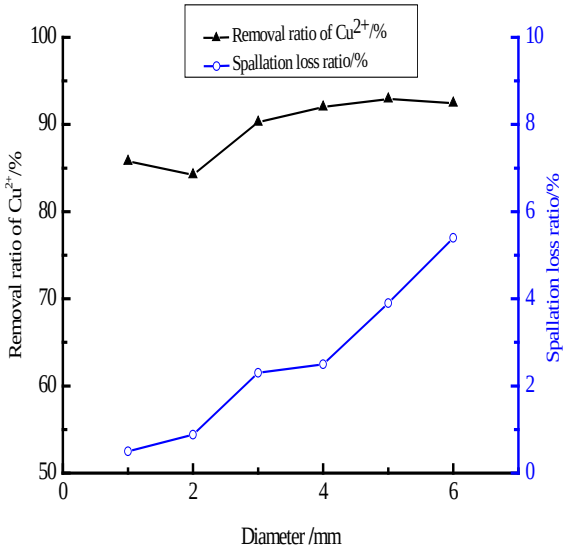

Fig.4 Effect of granulated diameter on removal efficiency

Fig.4 showed that spallation loss ratio and adsorption rate both increased with the increasing of granulated diameter because broken granules increase the surface area. Spallation loss ratio was lower and adsorption rate was higher with smaller granulated diameter. The smaller granulated diameter was，the better adsorption rate. However, there was a problem in practical artificial granulation, so the appropriate granulated diameter was of 1~2mm.

III. ANALYSIS OF PHYSICAL CHARACTERISTICS

The experimental results showed that the optimum technological conditions of preparing composite granules adsorbent materials were as follows: the mixture ratio of montmorillonite and fly ash was 6:4; the calcination temperature was 450℃; the proportion of additive was 10% of the mass of mixture; the diameter of the granular was 1～2mm. Granular adsorption materials of montmorillonite/fly ash were manufactured by the above technological conditions. Water adsorption capacity of granules, apparent porosity and bulk

density were measured by the hydrostatic weighing method. Compressive strength was measured by radial compressing technique and surface area by BET method. The test results are shown in Table 5.

TableV PHYSICAL CHARACTERISTICS OF GRANULATED ADSORPTION MATERIAL OF MONTMORILLONITE AND FLY ASH

Physical property	Test result
Water adsorption capacity (%)	31.80
Apparent porosity (%)	46.82
Bulk density (kg/m^3)	1.47
Compressive strength (MPa)	5.28
Surface area（m^2/g）	10.28

IV. CONCLUSIONS

The above experimental results showed that several factors such as the mixture ratio of montmorillonite and fly ash, the temperature of calcination and the additive proportion had certain influence on intensity and adsorption rate for the granulated composite materials. By comprehensive consideration of the adsorption properties and strength of granules, the optimum technological conditions of preparing the composite granules were determined as follows: the mixture ratio of montmorillonite and fly ash was 6:4; the calcination temperature was 450 ℃; the proportion of industrial starches was 10%; the diameter of the granular was 1～2mm. Using the composite particles prepared by the above technological conditions to treat wastewater containing 200mg/L Cu2+ initially, the adsorption rate could reach 96.34% and the spallation loss ratio was very low. Physical tests and analysis of this materials showed that the water adsorption capacity was 31.80%, the apparent porosity was 46.82%, the bulk density was 1.47 kg/m3, the compressive strength was 5.28 MPa, and the surface area was 10.28m2/g. The composite adsorbent materials prepared under the above conditions exhibited high adsorptive performance.

REFERENCES

[1] Shi Hui-sheng, Liu Yan-hong. Adsorption Characteristics of Bentonite to Pb~(2+),Zn~(2+),Cr(VI),Cd~(2+)[J]. Journal of Building Materials, 2006，9（5）：507－510

[2] Zhang Ling-yan, Yu Jia, Lin Xiu-ling. Preparation of Montmorillonite Granule Adsorbent[J]. Urban Environment &Urban Ecology, 2006，19（6）：24-25

[3] Shaobin Wang, Mehdi Soudi, Li Li, Z.H. Zhu. Coal Ash Conversion into Effective Adsorbents for Removal of Heavy Metals and Dyes from Wastewater[J]. Journal of Hazardous Materials, 20 May 2006, Pages 243-251

[4] Serpil Cetin, Erol Pehlivan. The Use of Fly Ash as A Low Cost, Environmentally Friendly Alternative to Activated Carbon for the Removal of Heavy Metals from Aqueous Solutions[J]. Physicochemical and Engineering Aspects, 20 April 2007, Pages 83-87

[5] K.S. Hui, C.Y.H. Chao',S.C. Kot. Removal of Mixed Heavy Metal Ions in Wastewater by Zeolite 4A and Residual Products from Recycled Coal Fly Ash[J]. Journal of Hazardous Materials,_9 December 2005, Pages 89-101

[6] I.J. Alinnor. Adsorption of Heavy Metal Ions from Aqueous Solution by Fly Ash[J].Fuel, March-April 2007, Pages 853-857

[7] Wu Ping-xiao. Clay Mineral Materials and Environmental Remediation[M]. Beijing: Chemical Industry Press, 2004.4-23

[8] Chen Peng. Study on Preparation of Layered Silicate Mineral Materials of High Absorbability for Heavy Metal Irons[D]. Wuhan: Wuhan University of Technology, 2007: 1-46

[9] Qin Fei, Xu Ou-yong, Jiang Ting-da. Preparation of Compound Granulated Adsorbent of Attapulgite and Studies on Its Adsorbability to Lead[J]. Chinese Journal of Environmental Science, 1996，17(4):47~50. 2003，(6):14-17

[10] Ma Wan-shan, Yang Ying-Qin, Ma Yan. Research on the Adsorption Property of Porous Granular Zeolite for Zn~(2+) [J]. Multipurpose Utilization of Mineral Resources, 2003，(6):14-17

[11] Research on the Adsorption Property and Regeneration of Porous Granular Zeolite for Cd~(2+) [J]. Non-metallic Mines, 2002，25(3):46-47

[12] Wang Hu-kun, Gong Wen-qi, Hu Jing. Treatment of Heavy-metal-containing Wastewater with Granulated Adsorbing Material of Fly Ash and Rectorite [J]. Journal of Wuhan University of Technology, 2007，29（8）：62-66

Comparison of Optical Properties of Bulk and Nano Crystalline Thin Films of CdS Using Different Precursors

Ruby Das[#1], Suman Pandey[*2]
[#]Department of Applied Physics, Bhilai Institute of Technology,
Durg, Chhattisgarh Swami Vivekanand Technical University,
[*]Department of Applied Physics,Rungta College of Engineering & Technology,
Bhilai,Swami Vivekanand Technical University,
[1]dwijendrad@yahoo.co.in, [2]sumu_74@rediffmail.com

Abstract-**The optical properties of bulk as well as nano CdS thin films developed by the Chemical Bath Deposition (CBD) were investigated in this paper. Results of optical Transmission, absorption, reflection spectra, optical conductance, refractive index, extension coefficient, real and imaginary dielectric constants studies are reported. The optical properties were obtained using UV-VIS Double Beam Spectrophotometer Version 6.51 in the wavelength range 200-1100 nm. The optical transmittance of the film of nano CdS formed at 50^0C was 99% at wavelength ≈ 475nm then decreases to 90% at wavelength ≈482nm for thin film of nano CdS at room temperature and 75% transmittance at wavelength ≈490nm for thin film of bulk CdS. The band-gap was also calculated from the equation relating absorption co-efficient with the wavelength. The energy band gap changes from 2.5eV (Bulk CdS) to 3.6eV (nano CdS at 50^0C). The plotted graphs show the optical characteristics of the film which varied with the wavelength and the photon energy. The optical conductance and band-gap indicated that the film is transmitting within the visible range. The dielectric constant and optical conductance of the film initially increases slowly then abruptly and finally becomes constant with increase in photon energy. The extinction coefficient and refractive index of the films also evaluated, which affected with the change in transmittance. The dielectric constant changes with change in photon energy.**

Keywords-**Chemical bath deposition; transmittance; absorbance; reflectance; band-gap; dielectric constant; refractive index; extinction coefficient; CdS**

I. INTRODUCTION

Currently there is a great deal of interest in optical and structural properties of nanometer sized semiconductor particle or thin films [1].CdS has intermediate energy band gap, reasonable conversion efficiency, stability and low cost therefore it is one of the most widely used material for CdS/CdTe and CdS/Cu_2S hetrojunction solar cells or device applications [2]. Nanocrystalline thin films of II-VI semiconductor have attracted particular attention, because they are relatively easy to synthesis in the size range required for quantum confinement. They are currently of great interest for their practical applications such as zero- dimensional quantum confined material, and in optoelectronics and photonics. Numerous reports are available in the literature on synthetic techniques as well as potential applications of nano-sized semiconductor particles [3]-[7] They show significant departures from bulk optical and structural properties when scale of confinement approaches to excitonic Bhor radius which sets the length scale for optical process [8]. CdS is a wide band gap semiconductor with Eg2.4eV [9]. The optical properties of CdS have been extensively studied [10]. Reduction in particle size strongly influences the crystallinity of the film. The thickness of the film was observed about 34.8nm when film was annealed at 360^0C for 1 hr[11]. CdS thin film have been fabricated using several deposition techniques such as screen printing [8], electro deposition [9], molecular beam epitaxy(MBE)[1], physical vapor deposition[10]. All these techniques require high sophisticated instrument and mismatch of thermal expansion coefficient between the film and substrate cause micro cracks. One of the promising techniques for producing large areas of inexpensive CdS film is chemical bath deposition and here we followed this method to synthesis the CdS films.

II. EXPERIMENTAL DETAILS

A. *Preparation of Bulk CdS Thin Film*

Bulk CdS thin films were prepared by Chemical Bath Deposition method from aqueous solution containing cadmium chloride (0.01M), zinc chloride (0.1M), thiourea (0.1M), 25% ammonia solution and triethanolamine (TEA) as a capping agent. The chemical bath is prepared from $CdCl_2$ solutions and 4% of the volume of the metal precursors, triethanolamine. The solution is stirred well for 5 minutes and required amount of ammonia solution (25% of NH_3 solution) was added to get a pH value 11. After proper stirring the solution with homogenizer for 10 minutes at the rate (125 rpm), thiourea is added into it and the reaction mixture was kept in a water bath at 50^0C. Before the deposition of cadmium sulphide on glass slides, the slides (substrate) were degreased in hydrochloric acid (HCl) for 24 hours, cleaned in detergent/cold water, and then rinsed with distilled water and allowed to drip dry in air. The substrate immersed vertically in the chemical bath and the deposition was carried out for 60 minutes. After the deposition, the films were rinsed in distilled water and dried in open air at room temperature.

$$CdCl_2 + (NH_2)_2CS + 2H_2O \rightarrow CdS + 2NH_4Cl + CO_2$$

B. *Preparation of Nano CdS Thin Films*

1) Nano Cds Thin Film at Room Temperature

Nano CdS thin film was prepared from aqueous solution of cadmium sulfate (1M) as a source for cadmium, thiourea (1M) as the source of sulphur and NH_4OH solution. The Chemical bath is prepared from the solution of $CdSO_4$ and $(NH_2)_2CS$. The solution is stirred well for 5 minutes and required amount of NH_4OH is added to get pH of 10.25. The solution was stirred with homogenizer continuously at the rate (125 rpm). A cleaned glass substrate (were degreased in hydrochloric acid (HCl) for 24 hours, cleaned in detergent/cold water, and then rinsed with distilled water and allowed to drip dry in air) was immersed vertically in the chemical bath and the deposition was carried out for 60 minutes. After the deposition, the films were rinsed in distilled water and dried in open air at room temperature.

2) Nano CdS Thin Film at 500C Temperature

Nano CdS thin can also prepared with the same precursors with the same preparation method for 60 minutes deposition at different bath temperatures of 50°C, 60°C and 80°C but the best result obtained at 50°C with smooth, uniform thin film deposition was carried out.

$$CdCl_2 \rightarrow Cd^{2+} + 2Cl^-$$

$$NH_4OH \rightarrow NH_4^+ + 2OH^-$$

$$Cd^{2+} + 2OH^- \rightarrow Cd(OH)_2$$

$$2NH^{4+} + 2Cl^- \rightarrow 2NH_4Cl$$

$$(NH_2)_2CS + Cd(OH)_2 \rightarrow CH_2N_2 + 2H_2O + Cd^{2+} + S^{2-}$$

$$Cd^{2+} + S^{2-} \rightarrow CdS$$

Overall reaction:

$$CdCl_2 + (NH_2)_2CS + 2NH_4OH \rightarrow CdS + CH_2N_2 + NH_4Cl$$

III. RESULTS AND DISCUSSION

A. UV Spectral Studies

1) Optical Transmittance Spectra

The transmittance spectrum of samples is taken by UV-VIS Double Beam Spectrophotometer Version 6.51 in the wavelength range 200-1100 nm. The UV spectra of the material provide important information about the details related with optical band. Fig.1 shows the wavelength dependence transmittance of the films of bulk and nano material CdS in the wavelength range 300nm-900nm.

The optical transmittance of the film formed at 50°C was about 99% at wavelength 475nm then decreases to 90% transmittance at wavelength 482nm and of 75% transmittance at wavelength 490nm for thin film of bulk CdS. The optical transmittance increases from bulk to nano CdS thin film at 50°C. It is observed that the transmission spectra shift towards shorter wavelength as the particle size decreases which suggest the increase in optical energy band gap. It is supposed that the tightly adherent collides are formed with the change in micro to nano particle size.

The optical absorption coefficient (α) was evaluated by Tauc relation $\alpha h\nu = A(h\nu - E_g)^n$ $\alpha = 2.3026\frac{A}{t}$, where A is constant called absorption coefficient, t is the film thickness, hν is the photon energy $(\nu = \frac{c}{\lambda}$, E_g is the band gap and n=1/2 for allowed direct transition.

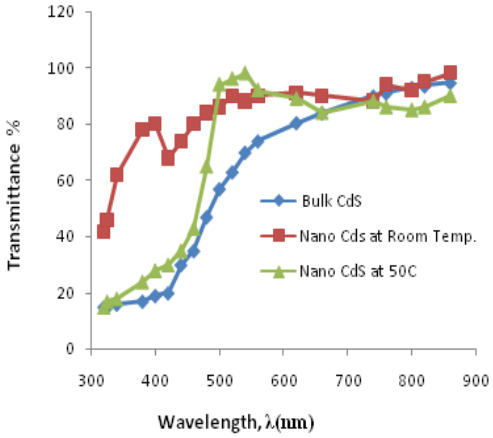

Fig.1. Transmittance Spectra of Bulk & nano CdS thin films

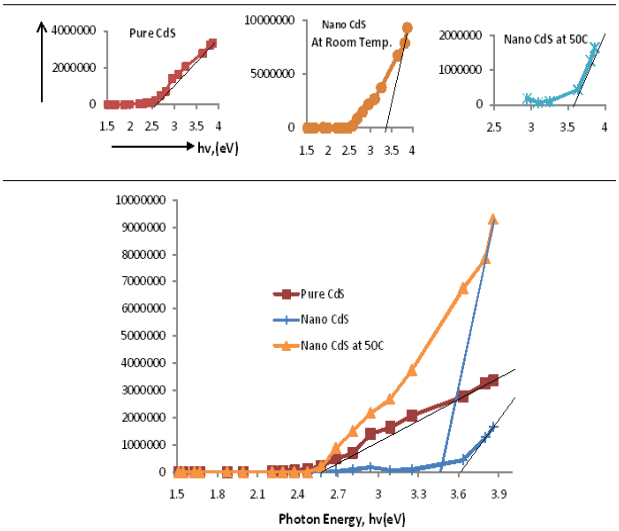

Fig.2 Plot between (αhν)2 and hν for different deposition conditions for band gap measurement.

Plotting the graph between $(\alpha h\nu)^2$ versus photon energy $(h\nu)$ gives the value of direct band gap. The extrapolation of the straight line to $(\alpha h\nu)^2 = 0$, gives the value of band gap, shown in Fig.2. From the UV spectra, it is clear that the absorbance decreases with increase in wavelength. This increase in transmittance indicates the presence of optical band gap in the material. The optical band gap of the films increases from 2.5eV to 3.6 eV from bulk to nano CdS thin films. The difference in the optical band values achieved was mainly due to the difference in the deposition techniques employed and the process parameter maintained during the growth of the films.

The band gap increases from bulk CdS to Nano CdS at 50°C. The highest blue shift energy is found to be 1.18eV. From the band gap information, the size of the CdS quantum dots were calculated using Effective Mass Approximation (EMA) method and Hyperbolic Band Model (HBM) using the following equations[12]:

$$E_{gn} - E_{gb} = \frac{\hbar^2 \pi^2}{2R^2 m^*}$$

and for HBM

$$E^2_{gn} = [E^2_{gb} + 2\hbar^2 E_{gb} (\pi / R)^2 / m^*]$$

In the above two equations, m* is the effective mass of the specimen, E_{gb} is the bulk band gap and E_{gn} is the band gap of the sample.

2) Optical Absorbance Spectra

Optical absorbance against the wavelength is observed for CdS thin films in the wavelength range 300–900 nm with glass as the reference and is shown in Fig.3.

The ratio of radiant power transmitted (P) by a sample to the radiant power incident (P_0) on the sample is called the transmittance T:

$$T = \frac{P}{P_0}$$

But, $P = P_0 e^{\alpha t}$

Where t is the thickness and $\alpha = (h\nu - E_g)^{1/2}$

We have $T = e^{\alpha t}$ or $\alpha = 2.303 \frac{A}{t}$

Therefore using the fundamental relation of photon transmission and absorbance the Absorbance (A) is defined as the logarithm (base 10) of the reciprocal of the transmittance.

$$A = \log_{10} \frac{1}{T} \text{ or } A = -\log_{10} T = -\log_{10} \frac{P}{P_0}$$

The absorbance spectrum shows a sharp increase in absorption at wavelength near to the absorption edge of the threshold wavelength for onset of absorption, the energy corresponding to this determines the band gap of the semiconductor material. The CdS film shows absorption coefficient (α) of about 1.4×10^{-6} m^{-1} near the absorption edge of wavelength 600 nm for bulk CdS , 1.48×10^{-6} for nano CdS thin film near the edge of wavelength 500 nm at room temperature and 2.5×10^{-5} for nano CdS thin film near the edge of wavelength 420 nm at 50°C .This shows that the deposited semiconductor films have a direct band gap material. It is observed that the absorption edge shifts towards shorter wavelength from bulk CdS thin film to nano CdS thin film at 50°C. The absorption onset in CdS-PVK thin film obtained at 300nm, gives band gap of 4.13eV [13].

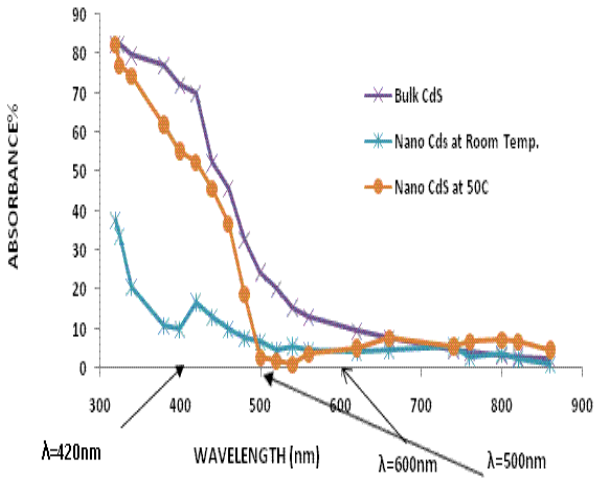

Fig.3. Absorption Spectra of Bulk & nano CdS Thin films

3) Optical Reflectance Spectra

If T is the Transmittance and A is the absorbance of the film then, the reflectance of the film has been found by using relationship.

$$R + T + A = 1 \text{ or } R = 1 - (T + A)$$

The reflectance of the bulk thin film initially increases with increase in wavelength up to 500nm after that it decreases up to 900nm due to increase in transmittance.

TableI VARIATION OF SIZE WITH DIFFERENT COMPOSITIONS FOR 60 MIN. DEPOSITIONS

Table 1- Variation of size with different Compositions for 60 min. deposition.

Composition	λ(nm)	Band Gap, Eg(eV)	Blue Shift Energy(eV)	Transmittance (T%)	EMA(nm)	HBM(nm)
Bulk CdS	490 nm	2.5	0.08	75%	9.72 nm	13.6 nm
Nano CdS	482 nm	3.2	0.78	90%	2.77 nm	3.5 nm
Nano CdS at 50C	475 nm	3.6	1.18	100%	2.53 nm	3.2 nm

The nano CdS thin film at room temp decreases up to 400nm then increases abruptly of 15% and after that it decreases with increase in wavelength. The reflectance of the nano CdS at 50°C initially increases up to 480nm after that it decreases abruptly up to 530nm then increases slowly with increasing wavelength up to 650nm then again decreases and shows parabolic path up to 900nm because of change in transmittance The reflectance is high (20%) in near infrared and visible region shown in Fig.4.

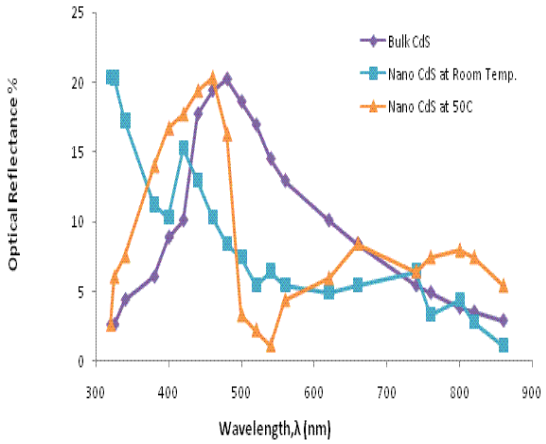

Fig.4 Reflectance Spectra of Bulk & nano CdS Thin films

B. Optical Conductance

The optical conductance is obtained using the relation,

$$\sigma = \alpha n c \varepsilon_0 \quad \text{or} \quad \sigma = \frac{\alpha n c}{4\pi}$$

Where σ is the optical conductance, c is the velocity of the radiation in the space; n is the refractive index and α is the absorption coefficient.

Fig.5 shows the variation of optical conductivity with the incident photon energy. The increased optical conductivity at high photon energies is due to high absorbance of CdS film in that region. The optical conductance and band gap indicated that the film is transmittance within the visible range [14].

The conductivity is constant up to 2eV of photon energy after that it increases with increase in photon energy. This shows that when the absorption of photon by film increases in that region. The conductivity peak of the films increases from bulk to nano CdS thin films.

C. Refractive Index

The refractive of the film has been calculated by knowing reflectance that can be determine by formula [15]:

$$R = \frac{(n-1)^2}{(n+1)^2}$$

Where, R is the normal reflectance.

Using this relation refractive index n can be determined by the formula:

$$n = \frac{[(R^{1/2})-1]}{[(R^{1/2})+1]}$$

Fig.6 shows the variation in the refractive index with the incident photon energy. The refractive index of the bulk CdS thin film initially increases with increase in photon energy up to 2.6eV after that it decreases with increase in photon energy due to increase in reflectance. The refractive index of nano CdS thin film deposited at room temperature increases exponentially with increase in photon energy where as the refractive index of the nano CdS thin film deposited at 50°C initially decreases then increases and finally decreases with increase in photon energy due to change in reflectance of the film.

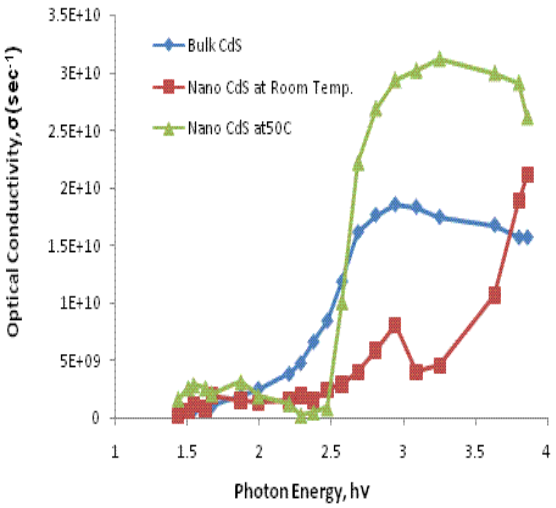

Fig.5 Optical Conductivity of Bulk & nano CdS Thin films

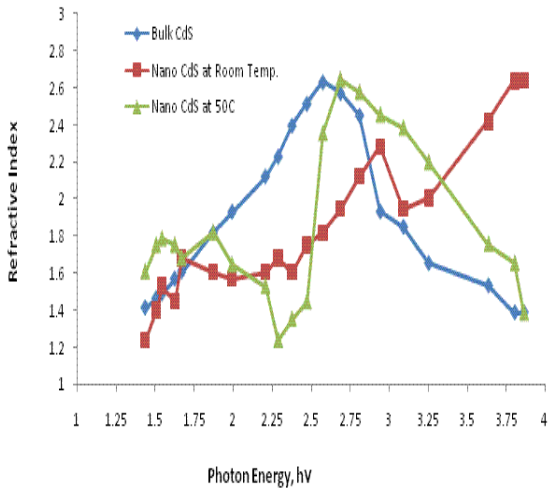

Fig.6 Change in Refractive Index with photon energy of CdS thin films.

D. Extinction Coefficient

The extinction coefficient allows for estimation of the molar concentration of a solution from its measured absorbance.

The extinction coefficient can be determine by using the relation, $k = \frac{\alpha\lambda}{4\pi}$, where λ is the wavelength of light.

Fig.7 shows the plot between photon energy Vs extinction coefficient. The extinction coefficient increases with increasing photon energy up to 2.8 eV then it becomes almost constant for bulk CdS thin film. It increases with photon energy up to 2.8eV then decreases slightly for nano thin film of CdS at room temperature. It again increases with photon energy. Nano thin film at 50^0C initially decreases up to 2.3 eV then increases with photon energy from 2.3eV to 4eV, which shows that the absorbance coefficient increases or transmittance increases or film thickness decreases because $\alpha = \log\frac{T}{t}$, t is the film thickness.

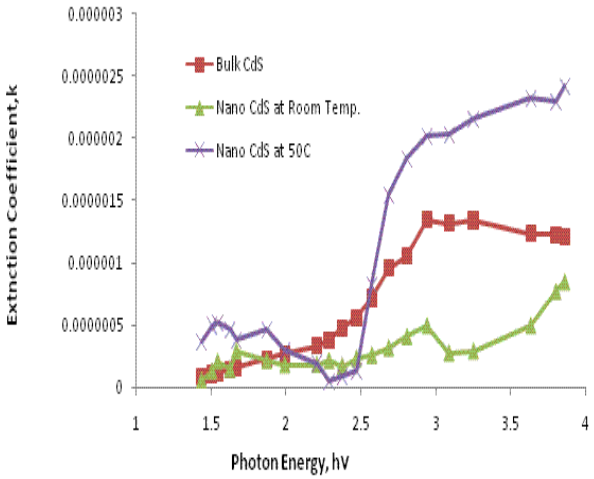

Fig.7 Change in Extinction Coefficient with photon energy of CdS thin films.

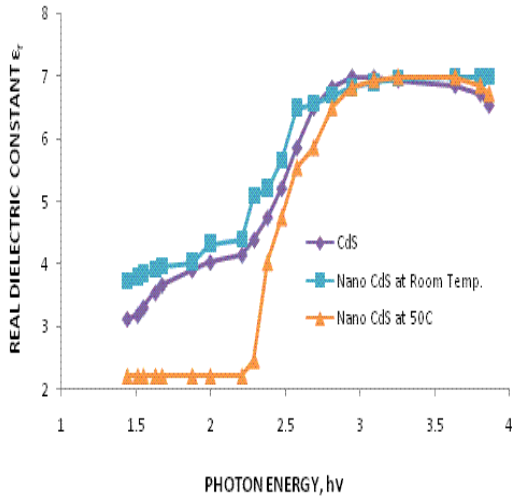

Fig.8. Plot between photon energy (hv) and Real Dielectric Constant.

E. Dielectric Constant

The dielectric constant and absorption coefficient are related and can be obtained theoretically with the relation given by the following: [Ugwu, 2006; Okujagu, 1992; Parachiniet et al., 1980; Chalkwski, 1980; Born et al., 1970; and Jenkins et al., 1976].

$$\varepsilon_r = n^2 - k^2 \text{ and } \varepsilon_i = 2nk$$

Where (ε_r) the real part of the dielectric constant, (ε_i) is is the imaginary part of the dielectric constant, (n) is the refractive index of the material and (k) is the extinction co-efficient given by:

$$k = \frac{\alpha\lambda}{4\pi}$$

Where (**α**) is the absorption co-efficient and (**λ**) is the wavelength of the radiation.

Fig.8 shows a plot between photon energy and real dielectric constant

$$\varepsilon_r = n^2 - k^2$$

The real part of the dielectric constant (shown in Fig.8) almost constant up to 2.24eV and increases slowly with photon energy 2.25eV then increases up to 2.8eV after that it again becomes constant up to 3.8eV.

The imaginary part of dielectric constant $\epsilon_i = 2nk$, represents the absorption associated of radiation by free carriers.

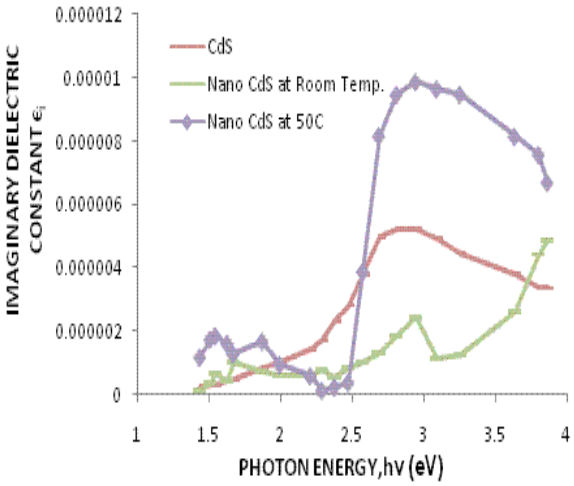

Fig.9. Plot between photon energy (hv) and Imaginary Dielectric Constant.

In metals imaginary part is always positive and represents loss factor or energy absorbed. The plot of imaginary part of dielectric constant as function of energy (shown in Fig.9) is initially increasing exponentially then decreases after 2.8eV to 4eV for bulk CdS thin film. The imaginary part of nano CdS at room temperature increases with increase in photon energy but the imaginary part of CdS initially decreases up to 2.5eV then increases exponentially up to 2.8eV then decrease slowly up to 4eV of photon energy. Imaginary part of dielectric constant is also related to conductivity so we can infer that energy lost to the metals appears as conductivity, but then it is directly proportional to conductivity but conductivity plots (as function of energy again) shows structures.

IV. CONCLUSIONS

This work has clearly presented how CdS thin films of bulk and nano material was grown using Chemical Bath Deposition techniques and how the effect of the solid state properties on spectral absorbance, transmission, and reflectance were obtained. The behavior of the film as illustrated in the graphs shows that the film is a visible transmitting thin film.The absorbance at the near infrared domain is low with high transmittance at the same region. The data explain the relationship between extinction coefficients, refractive index, real and imaginary dielectric constants and optical conductance.

ACKNOLEDGEMENT

The authors are thankful to the Management, Bhilai Institute of Technology, Durg, (C.G.) for providing all the facilities in lab.

REFERENCES

[1] R. Banerjee, R. Jayakrishnan, P Ayyub, J Physics Condens Matter 12, 10647 (2000).

[2] G. Brusatin, M. Guglielmi, P. Innocenzi, A. Martucci, G. Scarinci, J. Electrocer. 151,4(2000)

[3] M. Tamborra, M. Striccoli, R. Comparelli, M. L. Curri, A. Petrella and A. Agostiano, Nanotechnology 15, 5240(2004)

[4] N. Tessler, V. Medvedev, M. Kazes, S. Kan and U. Banin, Science 295, 1506 (2002)

[5] L. Klimov, A. A. Mikhailowsky, S. Xu, A. Malko, J. A. Hallingsworth and C A Leatherdole, Science 290, 340 (2000)

[6] D Battaglia and X Peng, Nano Letter. 2, 1027 (2002)

[7] [M. Abdulkhadar and Binny Thomas, Nano Structured Material. 5, 289 (1995)

[8] J. Nanda, K. S. Narayan, Beena Annie Kuruvilla, G. L. Murthy, D. D. Sharma, Applied Physics, 72, 11(1998).

[9] L Brus, Applied Physics, A53, 465 (1991).

[10] K. Nanda, S. N. Sarangi, S. N. Sahu, Nano Structured Material, 10, 1401(1998).

[11] Z.Rizwan, B.Z. Azmi, M.G.M. Sabri, optoelectronic and advanced materials 5, 4,(2011), 393-397.

[12] Shikha Tiwari and Sanjay Tiwari, Crystal Research Technology, 41, 82,(2006).

[13] P.Chouksey, B.P. Chandra, M. Rakhiyani, Indian J of Engg. And Material science 16,2009,157-160.

[14] E.I. Ugwa,,D.U.Onah, The pacific journal of science and technology 8, 1, 2007, 155-161.

[15] M. Y. Nadeem, W. Ahmed, Turk J. Phy, 24 ,651-659,(2000).

The Use of Electrochemical Impedance Spectroscopy to Monitor Delaminations in Polymer Matrix Composites: A Review

Drew A. Pavlacky[a], Victoria Johnston Gelling[b], and Chad A. Ulven[a]

[a]Department of Materials and Nanotechnology, North Dakota State University, Fargo, North Dakota

[b]Department of Coatings and Polymeric Materials, North Dakota State University, Fargo, North Dakota

drew.pavlacky@ndsu.edu,v.j.gelling@ndsu.edu,chad.ulven@ndsu.edu

***Abstract*-A review on the use of electrochemical impedance spectroscopy (EIS) was performed to determine the applicability of using this method as another method of non-destructive evaluation on polymer matrix composites. The motivation of this review is to display that EIS can be a quicker, more reliable, and quantitative method for use on a class of materials which has become increasingly more utilized in high profile applications. Conductive fiber composites comprise the bulk of the study as the traditional EIS methods correlated nicely as one constituent of the measurement setup must be conductive. For this class of material, several delamination mechanisms were studied including: fatigue, absorption of solutions, and application of overpotentials, galvanic coupling, and microbial attack. Also, non-conductive polymer matrix composites were also studied via a two electrode EIS technique. It was determined that EIS is an applicable method for determining delaminations from degradation stimuli. Also, in some instances the EIS response could be an indication to the extent of influence on mechanical properties.**

Keywords-Polymer matrix composites; Non-destructive evaluation; Electrochemical impedance spectroscopy; Delaminations; Carbon fiber reinforced composites

I. INTRODUCTION

Advanced polymer matrix composites (APMCs) have become increasingly popular in military and aerospace applications due to their low weight and high specific properties. APMCs are typically defined by the incorporation of long, high strength fibers (carbon, aramid, etc.) in an advanced matrix material (epoxies, phenolic, etc.). The combination of these two phases gives the manufactured composite superior mechanical and thermal properties.[1] In the 1970's and 1980's proposed designs of the AV-8B aircraft had 23.3% (by structural weight) epoxy matrix/graphite fiber in such critical areas as the fuselage and substructures of the wing.[2] The success these materials found eventually lead to use in the commercial sector of flight with the Airbus 340 and Boeing 777 which have 15% and 13% APMC materials by weight. [3] As APMCs move into the future, the uses in unmanned ground vehicles, unmanned air vehicles, and larger, more sophisticated commercial aircraft (i.e. Boeing 787) will be predominantly composed of composite materials.[1] The increased utilization of these materials comes not only from the weight savings and exceptional properties, but also the ease of manufacturing complex shapes as compared to monolithic metals. The emerging technologies of advanced composites manufacturing allow for these complex geometries to be manufactured with low void content, thus increasingly higher fiber volume fractions. [4]

APMCs' mechanical properties are highly dependent on establishing an intimate bond between the polymer matrix and fiber since the mechanical loading must be transferred from the matrix through the interface/interphase to the fiber.[5] However, once a composite is exposed to stimuli (mechanical forces, chemical reactions, fungal deterioration, etc.) the bond between fiber and matrix begins to become delaminated from one another and as the stimuli is repeated the delamination area augments.[6] A fairly similar phenomenon can be observed in the area of coated metals. Electrochemical impedance spectroscopy (EIS) is a widely accepted technique in the field of polymeric coatings for monitoring corrosion processes at the metal/coating interface.[7-8] Through the use of circuit modeling or simple spectra analysis, the delamination of coating from substrate can be observed over an exposure time from several types of external stimuli. [9] EIS can predict coating failure quite successfully before the visual signs can be interpreted. The quantitative measure is very useful when establishing guidelines of when failure can be assumed, and this can be done by monitoring the magnitude or complexity in shape of the Bode plots, or the onset of multiple time constants (i.e. another RC circuit in the circuit model) within the Nyquist plots. Another accepted approach of predicting coating failure is assessing the individual elements of circuit modeling over exposure time.[10] The quantitative nature of these measurements makes it an ideal candidate for non destructive evaluation (NDE) of polymer matrix composites as compared to that of qualitative measurements such as ultrasonic, thermography, acoustic emission, etc.

II. INVESTIGATING DELAMINATIONS IN CONDUCTING FIBER APMCS VIA ELECTROCHEMICAL IMPEDANCE SPECTROSCOPY

APMCs which contain carbon or graphite fiber in an insulating matrix have been studied to a higher degree than that of non-conductive fibers because the conductive fiber can act as the working electrode in the conventional three electrode EIS measurement, or if the fiber volume fraction is above the percolation threshold, the entire composite specimen may act as the working electrode. The latter is usually employed when dealing with the use of carbon fiber

reinforced plastics (CFRPs) for retrofitting concrete structures where EIS has been used to monitor delamination effects.[11-13] However, this subject will not be covered in this review article due to macro-scale delamination being monitored between the composite/concrete interface and not the matrix material and carbon fiber interface of the APMC.

With the APMCs, several modes of delamination progression have been studied over the past three decades which include: delamination by fatigue, delamination by solution absorption, delamination by overpotentials, delamination by galvanic coupling, and delamination by microbial matrix attack. For clarification, the following sections will be ordered by the degradation characteristic causing delamination and void creation.

A. Delamination Monitoring by EIS Measurements for Fatigued APMCs

The fatigue process in polymer matrix composites have been shown to create delaminations of fiber from matrix by several proposed mechanisms including fiber failure, fiber bridging, matrix cracking, etc.[14] In 1987, R.C. Glass, et al. examined the modeled double layer capacitance from the EIS measurement as an indicator of the extent of delamination of carbon fiber from an epoxy matrix after flexural fatigue was administered to the composite material.[15] The EIS measurements were carried out in typical three electrode technique with a saturated calomel electrode (SCE) acting as the reference electrode with a Luggin capillary probe. Carbon was utilized as the counter electrode with a deaerated sodium sulfate solution being the electrolyte solution. Investigation of the double layer capacitance after 10^5 fatigue cycles displayed significant decreases with respect to the original measurements. It was determined that this substantial change in measured capacitance could be accounted for by the corresponding decrease in the active electrode area caused by breakage of carbon fiber during fatigue. Also, flexural fatigue is a known method of increasing the absorption of solution in composite materials which would thus increase the respective capacitance which did not occur in this experimentation.[16] Both of these assumptions come from the established equation for capacitance displayed below.

$$C = \varepsilon_o \, \varepsilon_r \, A / d$$

Where ε_o is the permittivity of free space, ε_r is the dielectric constant, A is the active area, and d is the distance between the two conductive "plates". In this instance the area, A, would decrease due to fiber breakage causing a lower capacitance. However, if moisture is absorbed by the composite the dielectric constant would be of mixed permittivity which would be altered to a value between the polymer (2.1 – 12.2) and water (76.6 – 80.2) which would thus increase the capacitance.[17] This phenomenon was explained along with another interesting aspect that was observed after the initial fatigue testing was completed. It was detected that the measured capacitance from the EIS measurements continued to decrease even after the fatigue cycles were completed. This was attributed to the atmospheric moisture or electrolyte solution still present within the composite causing swelling of the polymeric matrix and continued fiber breakage of either partially damaged fiber or those fibers which have residual stresses from fatigue acting upon them again causing active area to decrease and therefore the measured capacitance. Further observation of the impedance spectra lead to the belief that fiber breakage was the main component of changes in capacitance since the resistance increased (i.e. shorter fiber and thus longer and less conductive pathways). From this work, it was discovered that fatigue caused several phenomenon to change the capacitance measured at the carbon fiber/epoxy matrix interface.

B. Delamination Monitoring by EIS Measurements for APMCs by Absorption of Solutions

The second focus of the article written by R.C. Glass et al. was to examine the effects of wet-dry immersion cycles of both distilled water and sodium sulfate.[15] The first EIS measurement was carried out in the as-received manner (if applicable), the second measurement was conducted after drying in an atmosphere of 140°C for 48 hours, the third measurement was performed after 30 days of immersion at room temperature (sodium sulfate) or 4 days at 100°C (distilled water), and the last measurement was conducted after repeating the procedure for the second measurement. Again it was observed that the capacitance decreased with immersion of both the distilled water and a sodium sulfate solution. However, after drying the composite sample and subjecting the sample to an EIS measurement, the capacitance had increased in almost every instance when compared to the EIS measurement after the first drying cycle. The results of the higher capacitance (in this instance) can be directly correlated to the delamination, microcracking and void formation caused in the composite sample during the drying cycle. These voids and delaminations make the access of testing electrolyte easier to the fibers causing increased area from an electrical bridging effect between fibers in a conductive solution. This claim is further reinforced as S.R. Taylor, et al. continued research in this area to determine that an unsized graphite fiber in epoxy would exhibit increases in capacitance when said fiber was exposed to a temperature of 90°C and immediately subjected to EIS measurements afterward.[18] The difference in coefficient of thermal expansions between the matrix and fiber caused areas of limited contact which when filled with testing solution caused an increase in the active area and thus the capacitance when compared to that of the unheated samples.

Lastly, a trend was observed between the capacitance and shear strength of the distilled water immersion samples. The results displayed the loss of shear strength of the carbon fiber containing composite samples correlate well qualitatively with the decrease in capacitance of the immersed samples. The correlation of the capacitance and shear strength can be observed in Figure 1. This further supports the postulation that the increase in weight (i.e. water absorption) may cause fiber breakage from polymeric swelling effects and therefore a decrease in mechanical properties.

Another solution was used by S.R. Taylor et al. in a study using different concentrations of sodium hydroxide solutions to produce hydroxyl (OH^-) ions for delamination creation in bismaleimide matrix/graphite fiber composites.[19] Hydroxyl ions were the proposed species that caused the delamination in

other studies exhibiting these composites to cathodic polarizations.

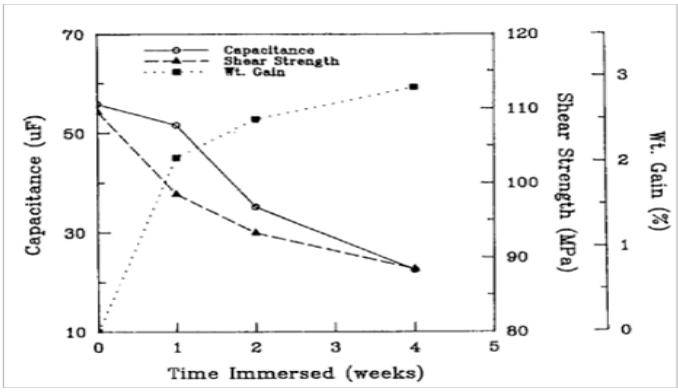

Figure 1 Relation of capacitance and weight gain to shear strength in immersion of composite sample in 90°C distilled water over exposure time

[Reproduced with kind permission from Springer Science+Business Media: Journal of Nondestructive Evaluation, Electrochemical impedance spectroscopy as a method to nondestructively monitor simulated in-service damage in a carbon fiber reinforced plastic, 6, 1987, 187, R.C. Glass, S.R. Taylor, G.L. Cahen, Jr., and G.E. Stoner,Figure 8.]

However, the results from the EIS measurements did not demonstrate a similar behavior to that of those exposed to cathodic polarization. The changes in phase angle plots for the caustic solution did not exhibit the behavior displayed by a "porous electrode" which can reveal the creation of delamination by changes in the phase angle over exposure time. The reason for this is that the dissolution of bismaleimide matrix was occurring in the bulk of the polymer, but not along the matrix/fiber interface which creates the voids and delaminations that can be measured by EIS. Also, if hydroxyl ions were being produced when impinged with cathodic potentials, the small pores and grooves would be imposed at the interface from the conducting species (i.e. graphite fiber) making it more likely to see the "porous electrode" effect.

C. Delamination Monitoring by EIS Measurements for Overpotentials

It is now well understood that carbon/graphite fiber with a glass cross weave polymer composites coupled with anodic acting metals creates a blistering effect at the surface of the composite material.[20-21] Blister formation is from evolving species created at the carbon fiber/polymer matrix interface during the electrochemical process induced by cathodic overpotentials. D. Kaushik et al. investigated the effect of applying cathodic overpotentials to carbon and glass fiber weave/vinyl ester matrix composites and monitoring these effects with EIS and the subsequent changes in modeled circuit elements.[22] The composite material was subjected to potentials of 0V, -0.65V, and -1.20V (vs. SCE) over various exposure times. To model this data, the proposed circuitry was initially established by F. Mansfeld and M.W. Kendig for coated metals that had exhibited the initiation of corrosion.[23-24] The models incorporated a two time constant circuit (i.e. two parallel resistor-capacitor circuits within the model) including solution resistance, R_s, "coating" capacitance, C_c, pore resistance, R_{po}, charge transfer resistance, R_{ct}, and a double layer capacitor, C_{dl}, or constant phase element. The main circuit element to monitor in this case, due to blister formation, was the pore resistance which could monitor the ease of electrolyte penetration. The results, in this instance, suggest that the electrochemical damage initiates at the carbon fiber/vinyl ester interface and moves outward toward the solution. This was proposed due to the resulting pore resistance values decreasing due to delamination and eventually void formation and these claims were reinforced by scanning electron micrographs. Also, pH measurements of the blisters were found to be very high due to the hydroxyl ions that were supposedly being produced within the composite structure. However, as mentioned previously S.R. Taylor et al., it is suggested that this hydroxyl ion was indeed formed, but may not be the key damaging species (the proposed damaging species will be covered later in this review article).[19]

M.N. Alias and R. Brown did a comparative study using a carbon and glass fiber weave in both epoxy and vinyl ester matrices, but the degradation procedure and analysis process were similar.[25-26] It was determined that the epoxy based composite experienced white deposit formation at the surface after varying lengths of cathodic potential exposure while the vinyl esters displayed blistering and black debris was found in the electrolyte solution. Circuit modeling of the EIS data suggested that a single resistor-capacitor circuit existed meaning the pore resistance was zero (i.e. a short circuit of electrolyte though the composite) for the epoxy composites at potentials less than -300 mV (vs. SCE). This could also be observed at the surface of the composites when more cathodic potentials than -300mV (vs. SCE) were applied to the samples. However, when the pore resistance was still detectable (i.e. voltage of -300 mV (vs. SCE) or more positive), it was determined that the values were higher in magnitude for the epoxy than the vinyl ester. Both composites exhibited damage dependent on the applied potential with more cathodic potentials causing greater damage by visual and electrochemical analysis. The impedance spectra displayed decreases in the magnitude with increased exposure time, and phase shifts (in frequency) toward lower frequencies with time. This work suggested possible degradation species at the -1200 mV (vs. SCE) to be the evolution of hydrogen to create the pores, or, due to the potential, direct reduction of the polymeric material.

A published article of S.R. Taylor's research in 1994 sought to determine the damage effects that occur when cathodic potentials and thus electrochemical processes are introduced at the matrix/fiber interface by looking at a the depth of penetration of a proposed "crevice" geometry between the matrix material and fiber.[27] This experimentation was conducted on a uni-directional bismaleimide matrix/graphite fiber composite which had EIS measurements conducted in typical three electrode fashion with the electrolyte being sodium chloride solution. Through extensive derivation, it was determined that the depth and width of the crevice could be monitored strictly by the phase angle which is measured during EIS experimentation. This derivation was originally proposed by de Levie to monitor the surface roughening of a scratch defect in electrodes for fast

electrochemical measurements.[28] Having graphite fiber act as one of the electrodes of the electrochemical system is beneficial since many of the underlying assumptions of the derivation are accurate due to its non-Faradaic region near the open circuit potential. Also, when surrounded in a polymeric matrix, a large portion of the impedance is due to the double layer capacitance observed when exposed to an electrolyte. Another advantage in using the phase angle to determine the penetration of delaminations is that the phase angle is an inherent parameter meaning it is independent of the area making this especially useful in laminate composites.

In order to create delamination effects, the author imposed cathodic potentials of -1.2V, -1.4V, and -1.73V (vs. SCE) in a 3.5% sodium chloride solution for varying amounts of exposure times. The potentials were maintained except when the specimens were being subjected to EIS experimentation which used the open circuit potential with a perturbation of 10 mV. The results of the penetration depth as a function of time for each voltage can be observed in Figure 2. As mentioned before, the most pertinent aspect of the impedance spectra was the phase angle which could be used in the series of equations derived to understand the depth of penetration of electrolyte (i.e. the length of delamination). It was observed that the larger overpotential caused greater lengths of delamination of the carbon fiber from the matrix material.

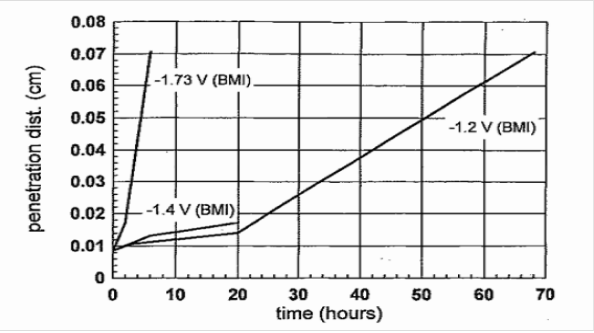

Figure 2 - Results of penetration depths of delamination calculated from the impedance phase angle data

[Reproduced by permission of The Electrochemical Society: Journal of The Electrochemical Society, The Detection and Analysis of Electrochemical Damage in Bismaleimide/Graphite Fiber Composites, 143, 1996, 451, S.R. Taylor, F.D. Wall, and G.L. Cahen, Jr., Figure 5.]

In order to calculate the penetration distance, several assumptions needed to be implied. For instance, the opening of the crevice (i.e. distance from fiber edge to polymer edge at surface) needed to be held constant even though this was known to change over time. Also, the value of the double layer capacitance was approximated from values suggested for the basal plane of graphite and crystal edges even though actual configuration was not determined during this study. Even with these assumptions, the extrapolated data to 12 months was very near to that found for actual data of epoxy/graphite fiber coupled with magnesium in seawater.

The findings through this experimentation were very beneficial for determining the delamination effects in graphite fiber composites when exposed to cathodic potentials which can be observed when these materials are coupled with common industrial metals in an electrolytic environment.

S.R. Taylor et al. continued this work to further explain the phenomenon observed involving cathodic potentials used with bismaleimide matrix/graphite fiber composites.[19] In this study, an understanding of the change in phase angle was studied in more detail. Since the phase angle is used to determine the depth of the delamination, the change in phase angles at corresponding frequencies can give better insight into the material's interfacial changes. Results revealed that with the more cathodic potentials the corresponding change in phase angle increases. Even though the -1.2 V and -1.4 V (vs. SCE) should be limited by diffusion processes, as defined by the potentiodynamic polarization data, the -1.4V results exhibited a larger change in the phase angle with increasing exposure time even though the imposed currents would be of the same magnitude and thus reactions at the interface should be similar. Further EIS experimentation was completed on samples that were exposed to smaller cathodic potentials ranging from -30 mV to -300 mV (vs. SCE). It was discovered that potentials ranging from 0 V to -100 mV (vs. SCE) exhibited phenomenon not observed in the other cathodic potentials, but once the -200 mV to -300 mV (vs. SCE) were measured the capacitance values again began to increase as expected. The explanation for the lower cathodic potentials behaving erratically was due to the composite sample's open-circuit potential varying up to 300 mV due to inhomogeneity in the sample and the sample's history. Also, the slight cathodic potential changes could create reduction of certain functional groups or electrostatic debonding at the interface between fiber and matrix. One of the most important findings of this work was the proposition of an alternative specie/species that cause the porosity to be created at the interface other than hydroxyl ions. From the change in phase angle results, a tail was observed at low frequencies in the cathodic potentials and that was not observed when hydroxyl radicals were readily present in solution immersion testing. This is believed to be caused by damage inherent from the generation of peroxide, superoxide radicals, and possibly hydroperoxyl radicals. Cleavage of the carbon-carbon bonds (amongst several other degradation mechanisms) within polymer matrices after reactions with oxy-radicals and peroxy-radicals has been well documented. [29-31] However, the degradation species have not been explicitly determined and is most likely to be different for each matrix material.

The application of anodic overpotentials was also investigated by S.R. Taylor et al.[19] Although the practical applications of having a very noble species such as graphite being subjected to an anodic overpotential is limited, it was suggested by the authors that this could indeed by the case if a stray current was administered to the composite. A large overpotential of +1.5 V (vs. SCE) was applied to the samples for 20 hours. Anodic polarization resulted in decrease in impedance magnitude with time, a shift of the capacitive region, in the impedance magnitude plots, toward lower frequencies, but very little depression in the amplitude of the phase angle peak. The shift in the impedance plots suggest the same activity that occurred in cathodic overpotentials, but the phase angle displayed little change in the low frequency phase angles, further reinforcing that the delamination or pore formations were not occurring.

D. Delamination Monitoring by EIS Measurements for Galvanic Couplings

Much like imposing cathodic potentials, coupling of carbon fiber composites with more active metals would produce similar effects in the presence of an electrolyte. S.R. Taylor also conducted experimentation to monitor the creation of delaminations when bismaleimide matrix/graphite fiber composites were coupled with aluminum, steel, copper, and titanium.[19] The results demonstrated similar, but not identical, trends observed when cathodic potentials were applied including impedances decreasing with time, the slope of the Nyquist plot decreasing, and phase angle measurements decreasing with increasing exposure time. As expected, the impedance changes were concurrent with the metal's electrochemical potentials in a sodium chloride containing solution with aluminum being most active at approximately -0.81 V (vs. SCE), next is low carbon steels at approximately -0.70 V (vs. SCE), then copper at approximately -0.20 V (vs. SCE), and lastly titanium at approximately -0.05 V (vs. SCE).[32] Again the phase angle decreasing with time was the main indicator that a "porous electrode" was being formed and the active area was increasing due to the formation of the peroxide radicals that degraded the polymer at the interface.

E. Delamination Monitoring by EIS Measurements during Microbial Attack

It has been shown that microbes tend to thrive off the additives (sizings, plasticizers, flame retardants, etc.) in carbon fiber reinforced composites, as it tends to be the site of microbe growth via scanning electron micrographs.[33] J.-D. Gu has provided research examining the relationship between growth of microbes at the carbon fiber/matrix interface using EIS as a technique to monitor the growth (and consequently the delamination of fiber from matrix) of these bio-organisms.[34-35] Graphite and glass fiber weave/epoxy matrix composites were manufactured and were then inoculated with a fungal consortium and then characterized by EIS and SEM after 179 days of incubation. EIS results displayed that the impedance magnitude was decreasing over exposure time while samples in non-microbe rich environments revealed increases after initial testing, but remained stable after initial testing. The shape of the impedance magnitudes exhibits both a decrease in the resistive and imaginary elements of the sample. This can be explained by both a decrease in the pore resistance (from microbe pathways) and an increase in the capacitive behavior due to increased active area which corresponds to a decrease in the imaginary impedance which is verified in the Nyquist plot. These observations were also visually verified using scanning electron micrographs.

III. INVESTIGATING DELAMINATIONS IN NON-CONDUCTING FIBER APMCS VIA ELECTROCHEMICAL IMPEDANCE SPECTROSCOPY

The use of a non-conducting fiber (i.e. glass, aramids, etc.) in an insulating matrix gives the overall composite an insulating nature. These materials are not necessarily suitable for electrochemical measurements to be performed upon them which is why very little research exists in this area. Nevertheless, the need for quantitative non-destructive measurement is still present as special-purpose fibers continue to be enhanced to the point of rivaling the strength and stiffness of carbon fibers. This enhancement of glass fibers has been observed in recent years with the development of several special purpose glasses including "S"-glass, "M"-glass, "C"-glass, etc.[36] Even though these fibers are not conductive, EIS can still be administered to the sample, but the use of a two-electrode technique must be used. In terms of non-conductive composites, the two electrode technique usually utilizes two electrodes of highly conductive metal. In this configuration, the working electrode (of the conventional three electrode set-up) will act as one of the metal electrodes and the counter and reference electrodes (of the conventional three electrode set-up) will be on the other metal electrode. A schematic representation of the two electrode technique is depicted in Figure 3.

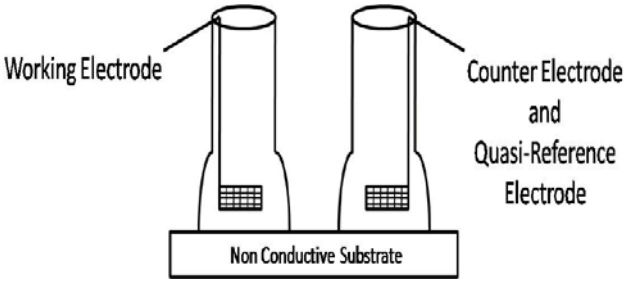

Figure 3 Schematic of the two electrode EIS setup

This technique has been shown to display similar trends to that of the three electrode set-up for coating systems which have undergone corrosion processes where point defects were not present.[37]

P.D. Fazzino, et al. researched the effects fatigue has on the impedance spectra for halogenated epoxy matrix/E-glass fiber composites.[38-39] By subjecting the composite material to fatigue mechanical loadings from cyclic compression, delaminations and voids were created. However, the first set of testing was to determine the effect immersion and drying would have on the overall electrochemical impedance spectra. By soaking the samples in water for 48 hours and then testing it intermittently while drying, it was determined that the spectra of the impedance magnitude changed from a resistor-capacitor circuitry to one dominated by the capacitive effect while drying. This could be explained by the inherent moisture of the soaked sample decreasing the resistance, thereby increasing the conductivity. Another preliminary study exhibited that the higher concentration of sodium chloride in solution decreased the impedance magnitude as the ion and electron movements were less restrained between the two electrodes. After initial studies, fatigued samples were then soaked in 3M sodium chloride solutions and measured in two electrode EIS fashion. A trend was observed explaining that with an increase in fatigue cycles a decrease in the impedance magnitude was observed. Figure 4 demonstrates the trend of decreasing impedance with increased fatigue cycles.

This is attributed to the phenomenon of void creation and delaminations causing increased solution uptake and thus less resistive pathways through the composite. Even for the

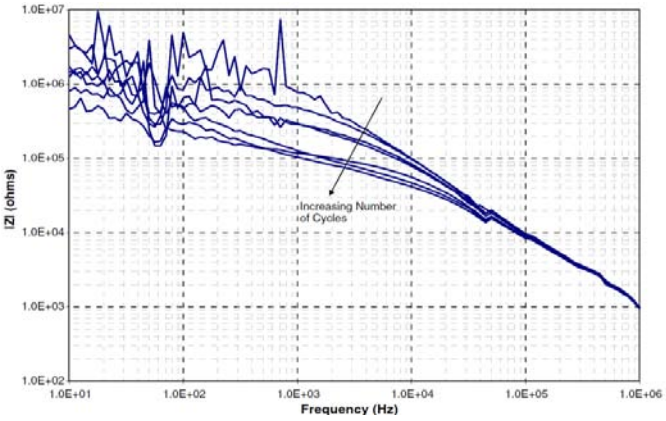

Figure 4 Decreasing impedance with increased fatigue cycles

[Reproduced with kind permission from Springer Science+Business Media: Journal of Nondestructive Evaluation, Electrochemical Impedance Spectroscopy Detection of Damage in Out of Plane Fatigued Fiber Reinforced Composite Materials, 15, 2008, 137, P. Fazzino and K. Reifsnider , Figure 12.]

smallest amount of damage (roughly 20% of the cycles to failure), visual damage was unnoticeable, but detectable by EIS measurements.

Further work by this group investigated the direction of fatigue on the impedance results. It was determined that composite materials cut in the 0° and 90° (with respect to the warp fiber orientation) displayed similar results because a plain weave was selected and is quasi-isotropic while an off-axis bending samples (cut in the 45° direction) revealed drastically different results. The first noticeable trend was that the impedance magnitude was significantly lower (by over two orders of magnitude) in the 45°, and the high frequency impedance was changing while in the 0° and 90° orientations the high frequency stayed relatively similar. These changes in impedance spectra can be attributed to the 45° orientation bending causing more matrix driven behavior and thus more microcracking and void creation was occurring within the matrix. This causes an increase in the quantity of hydration sites and thus less resistive pathways to the ions and electrons causing a decrease in the resistive and capacitive behaviors of the composite. The large shifts in the high frequency impedance also suggest that the resistive and capacitive behavior is changing substantially. More extensive investigation examined the relationship between elements of the impedance spectra, area of damage, and strain to break in tension as a function of the fraction of life. It could be observed that trends did exist between the impedance magnitude at 1000 Hertz and initial slope of the Nyquist and the mechanical strain to break. Normalizing the data values against their initial values revealed that a correlation can be observed among the mechanical failure (strain to break) and electrochemical impedance spectra (initial slope of Nyquist plot) making EIS a suitable non-destructive evaluation technique for this material and mechanical loading.

IV. CONCLUSIONS

As advanced polymer matrix composites become increasingly popular in military, aerospace, and industrial applications, the need for quantitative non-destructive evaluation is becoming more apparent. This review article examined the applicability of using electrochemical impedance spectroscopy as a means to non-destructively evaluate this class of materials. Delaminations of both conductive and non-conductive fibers from an insulating matrix can be examined with this technique. With carbon/graphite fiber, equations have been developed to monitor the apparent characteristics of the fiber acting in a "porous electrode" manner, which can be used to quantify the length, and subsequently the volume, of delaminations. Studies have also been used to understand the key damaging species of coupling these carbon fiber composites with metals, and though an exact species has not been agreed upon, it is known that the species is dependent upon the potential applied and the type of matrix material involved. With the use of the two electrode technique and a hydrated sample, the delamination effects can be monitored with electrochemical impedance spectroscopy on non-conductive composites and correlation of the spectra characteristics with the mechanical properties can also be approximated. Overall, this technique of non-destructive evaluation is versatile and can give quantitative trends as opposed to many non-destructive techniques which tend to only be qualitative by nature.

REFERENCES

[1] Strong, A., Fundamentals of composites manufacturing: materials, methods and applications. 2nd ed. 2008, Dearborn, MI: Society of Manufacturing Engineers.

[2] Watson, J. Preliminary design development AV-8B forward fuselage composite structure. in Fourth Conference on Fibrous Composites in Structural Design. 1978. San Diego, CA, USA: Plenum Press.

[3] Pilato, L. and M. Michno, Advanced composite materials. 1994: Springer-Verlag.

[4] Gutowski, T., Advanced composites manufacturing. 1997: Wiley New York.

[5] Agarwal, B., L. Broutman, and K. Chandrashekhara, Analysis and performance of fiber composites 3rd edition. 2006: Wiley New York.

[6] Sridharan, S., Delamination behaviour of composites. 2008: Woodhead Publishing.

[7] Mansfeld, F., Electrochemical impedance spectroscopy (EIS) as a new tool for investigating methods of corrosion protection. Electrochimica Acta, 1990. 35(10): p. 1533-1544.

[8] Amirudin, A. and D. Thieny, Application of electrochemical impedance spectroscopy to study the degradation of polymer-coated metals. Progress in Organic Coatings, 1995. 26(1): p. 1-28.

[9] Scully, J., D. Silverman, and M. Kendig, Electrochemical impedance: analysis and interpretation. 1993, West Conshohocken, PA: ASTM International.

[10] Lavaert, V., M. De Cock, M. Moors, and E. Wettinck, Influence of pores on the quality of a silicon polyester coated galvanised steel system. Progress In Organic Coatings, 2000. 38(3-4): p. 213-221.

[11] Davis, G., M. Rich, and L. Drzal, Monitoring Moisture Uptake and Delamination in CFRP-Reinforced Concrete Structures with Electrochemical Impedance Sensors. Journal of Nondestructive Evaluation, 2004. 23(1): p. 1-9.

[12] Hong, S., R. Harichandran, and F. PE, Sensors to monitor CFRP/concrete bond in beams using electrochemical impedance spectroscopy. Journal of Composites for Construction, 2005. 9: p. 515.

[13] Kim, S.D., C.W. In, K.E. Cronin, H. Sohn, and K. Harries, Reference-Free NDT Technique for Debonding Detection in CFRP-Strengthened RC Structures. Journal of Structural Engineering, 2007. 133(8): p. 1080-1091.

[14] Kelly, A. and C. Zweben, Comprehensive composite materials: Volume 2 Polymer Matrix Composites. 2000, Oxford, UK: Elsevier.

[15] Glass, R., S. Taylor, G. Cahen, and G. Stoner, Electrochemical

impedance spectroscopy as a method to nondestructively monitor simulated in-service damage in a carbon fiber reinforced plastic. Journal of Nondestructive Evaluation, 1987. 6(4): p. 181-188.

[16] Callinan, R., Environmental Effects on the Static and Fatigue Strength of Graphite/Epoxy Structures. Austrailian Department of Defense, Austrailian Aeronautical Research Labs, Melbourne, Australia, AD-A170 927. 1985.

[17] Lide, D., Handbook of chemistry and physics. 84th Edition ed. 2003: CRC Press LLC.

[18] Taylor, S., L. Melvin, T. Mangiacapre, G. Cahen Jr., and G. Stoner, Non-Destructive Method for Environmental Breakdown of Graphite Fiber Reinforced Polymer Composites. U.S.A.R. Office, University of Virginia, AD-A223 729. 1990.

[19] Taylor, S., F. Wall, and G. Cahen Jr, The detection and analysis of electrochemical damage in bismaleimide/graphite fiber composites. Journal of The Electrochemical Society, 1996. 143(2): p. 449-458.

[20] Tucker, W., R. Brown, and L. Russell, Corrosion between a graphite/polymer composite and metals. Journal of Composite Materials, 1990. 24(1): p. 92.

[21] Sloan, F. and J. Talbot, Corrosion of Graphite-Fiber-Reinforced Composites I Galvanic Coupling Damage. Corrosion, 1992. 48(10).

[22] Kaushik, D., M. Alias, and R. Brown, An impedance study of a carbon fiber/vinyl ester composite. Corrosion, 1991. 47(11): p. 859-867.

[23] Mansfeld, F., M. Kendig, and S. Tsai, Evaluation of corrosion behavior of coated metals with AC impedance measurements. Corrosion, 1982. 38(9): p. 478-485.

[24] Kendig, M., F. Mansfeld, and S. Tsai, Determination of the long term corrosion behavior of coated steel with AC impedance measurements. Corrosion Science, 1983. 23(4): p. 317-329.

[25] Alias, M. and R. Brown, Corrosion behavior of carbon fiber composites in the marine environment. Corrosion Science, 1993. 35(1-4): p. 395-402.

[26] Alias, M. and R. Brown, Damage to composites from electrochemical processes. Corrosion, 1992. 48(05).

[27] Taylor, S., A Nondestructive Electrochemical Method to Detect and Quantify Graphite Fiber/Polymer Matrix Disbondment in Aqueous and Cathodically Polarized Conditions. Composite Interfaces, 1994. 2(6): p. 403-217

[28] De Levie, R., The influence of surface roughness of solid electrodes on electrochemical measurements. Electrochimica Acta, 1965. 10(2): p. 113-130.

[29] Song, J. and C. Fischer, Thermal oxidative degradation of poly (methyl methacrylate). Polymer Degradation and Stability, 1992. 36(3): p. 261-266.

[30] Braun, D., S. Richter, G. Hellmann, and M. Rätzsch, Peroxy-initiated chain degradation, crosslinking, and grafting in PP-PE blends. Journal of Applied Polymer Science, 1998. 68(12): p. 2019-2028.

[31] Cao, H., J. Yuan, R. Zhang, C. Huang, Y. He, T. Sandreczki, Y. Jean, B. Nielsen, R. Suzuki, and T. Ohdaira, Degradation of polymer coating systems studied by positron annihilation spectroscopy. 3. Wavelength dependence of UV irradiation effect. Macromolecules, 1999. 32(18): p. 5925-5933.

[32] Jones, D., Principles and Prevention of Corrosion. 2nd ed. 1992, Upper Saddle River, NJ: Prentice-Hall.

[33] Gu, J.-D., Microbiological deterioration and degradation of synthetic polymeric materials: recent research advances. International Biodeterioration & Biodegradation, 2003. 52(2): p. 69-91.

[34] Gu, J.D., C. Lu, K. Thorp, A. Crasto, and R. Mitchell, Fiber-reinforced polymeric composites are susceptible to microbial degradation. Journal of Industrial Microbiology & Biotechnology, 1997. 18(6): p. 364-369.

[35] Gu, J., A. Crasto, K. Thorp, C. Lu, and R. Mitchell, Fungal Degradation of Fiber-Reinforced Composites Materials. Corrosion, 1996.

[36] Wallenberger, F. and P. Bingham, Fiberglass and Glass Technology: energy-friendly compositions and applications. 2010, New York, NY: Springer Science.

[37] Qi, X., Organic Coatings for Corrosion Protection. Thesis. North Dakota State Universtiy, Coatings and Polymeric Materials, 2009.

[38] Fazzino, P. and K. Reifsnider, Electrochemical Impedance Spectroscopy Detection of Damage in Out of Plane Fatigued Fiber Reinforced Composite Materials. Applied Composite Materials, 2008. 15(3): p. 127-138.

[39] Fazzino, P., K. Reifsnider, and P. Majumdar, Impedance spectroscopy for progressive damage analysis in woven composites. Composites Science and Technology, 2009. 69(11-12): p. 2008-2014.

Synthesis of Nanocrystalline Magnesium Ferrites Powder from Mill Scale

M. M. Hessien[1, 2]*, Z. I. Zaki[1,2], Q. Mohsen[1]

[1] Department of Chemistry, Faculty of Science, Taif University, Saudi Arabia

[2] Department of Central Metallurgical Research and Development Institute (CMRDI), Cairo, Egypt.

Department of Chemistry, Faculty of Science, Taif University, Saudi Arabia

hessienmahmoud@yahoo.com

Abstract **-Nano-crystalline magnesium ferrites powder were synthesized using mill scale via classical ceramic route. The effect of annealing temperature and Mg:Fe molar ratios (0.5, 0.55 and 0.65) on the formation of $MgFe_2O_4$ were studied. The results showed that the mole ratio of Mg/Fe and the annealing temperature were factors affecting the formation of $MgFe_2O_4$ in pure form. The magnesium ferrite formed were accompanied by a percentage of the iron oxide for the Mg:Fe = 0.5 and 0.55 for all studied annealing temperatures. The presence of iron oxide is very high at annealing temperature 1000°C and highly decreased with the raise of annealing temperature. A single phase of $MgFe_2O_4$ was formed at Mg:Fe=0.65 at 1200 °C. The nanocrystalline size of the prepared $MgFe_2O_4$ phase prepared was in the range of 170nm had good magnetic properties with maximum saturation magnetization (36.64 emu/g) at Mg/Fe mole ratio 0.65 and 1300°C.**

Keywords-*mill scale; magnesium ferrite; nanocrystalline; ceramic route*

I. INTRODUCTION

The ferrite material is a new advanced material which characterized by high magnetic permeability, high saturation magnetization and low power losses. These materials are extensively used in magnetic fluid, microwaves devices, magnetic recording media, and fabrication of radio frequency coils, transformer cores, and chock coils, noise filters, recording heading and rod antennas [1-3]. Mg ferrites belong to the normal, or the inverse, spinel structure ferrites group. Magnesium ferrite ($MgFe_2O_4$) has a cubic spinel-type structure [4, 5]. It is well known as -a soft magnetic n-type semiconductive material, with high resistivity and low magnetic and dielectric losses. These materials are extensively used in magnetic fluid, microwaves devices, magnetic recording media, and fabrication of radio frequency coils, transformer cores, and chock coils, noise filters, recording heading and rod antennas. In addition, Mg ferrites are very important in heterogeneous catalysis, adsorption and sensors [6, 7].

The magnetic properties of the ferrites depend on the microstructure [8, 9]. The microstructure of the ferrite is determined by a variety of factors; raw materials quality, annealing temperature, annealing time and the materials composition. This fact is very important because the microstructures developed during sintering are determined, to a large extent, by the powder's characteristics (crystallite size and shape, size distribution, porosity, state of agglomeration, chemical and phase composition), which are closely associated with the processing method [8, 9]. However, there is no many studies has been found in the literature correlating the microstructure and effect of grain size with the magnetic properties of Mg ferrite powders. This study, therefore, will investigate the effect of the sintering temperature (1000 - 1300°C) on the microstructure and magnetic properties of $MgFe_2O_4$ ferrites prepared by ceramic method.

On the other hand, during the heating of steel slabs before rolling in the steel-making process, their upper layer can be oxidized to iron oxide. This oxide is called "mill scale", and it is easily removed from the surface by a shower of water during the rolling of these slabs [10-13]. This mill scale can be considered as a valuable secondary raw material according to its high iron content, low impurities and stable chemical composition. The quantity of mill scale is increasing rapidly with the current demand of increasing world steel production. The high iron content of these materials with its very low impurities makes it an excellent source for soft and hard magnets preparation via its mixing with other metal oxides and further heat treatment at various temperatures.

From this point of view, the present investigation handled an economic route for using the ceramic technique in synthesis of magnetic nano-crystalline magnesium ferrite powder through solid-state reaction of a mixture consisting of secondary iron oxide resources with analytical grade magnesium oxide in different Fe/Mg mole ratios. The effect of firing temperatures as well as firing time on both physical and magnetic properties of the produced compacts will investigated.

II. EXPERIMENTAL

This paper aimed to handle an economic route for using the conventional ceramic technique in synthesis of magnetic nano-crystalline magnesium ferrite powder as soft magnetic materials for industrial and different magnetic applications. A mill scale sample with 70.1% total iron, 46.5% Fe^{2+}, 21.6% Fe_3O_4, 0.44% metallic iron, 0.52% SiO_2, 0.18% CaO, 0.084% Al_2O_3, 0.029% MgO, 0.02% S and 0.21% C was obtained from HADEED Saudi Iron & Steel Company(SABIC). Mill scale fines were finely ground to a mean particle size of

0.074 mm and then thoroughly mixed with stoichiometric amount of analytical grade magnesium oxide. A series of mill scale and magnesium oxide with various Mg:Fe molar ratios (0.5, 0.55 and 0.65) were prepared. The pre-calculated stoichiometric ratios of mall scale and MgO were mixed in a ball for 6 h and then dried at 100℃ overnight. For the formation of the Mg ferrite phase, the dried precursors (powders were calcined at a rate of 10 ℃/min in static air atmosphere up to the required annealed temperature and maintained at the temperature for the annealing time in the muffle furnace. The effect of annealing temperature (1000, 1100, 1200 and 1300 ℃) on the formation of Mg ferrite was studied while the annealing time was constant and kept 2 hours.

The crystalline phases present in the different samples were identified by X-ray diffraction (XRD) on a Brucker axis D8 diffractometer using Cu-K_α (λ =1.5406) radiation and secondary monochromator in the range 2θ from 10° to 80°. The crystallite size of magnesium ferrite present in the investigated was based on X-ray diffraction line broadening and calculated using Scherrer equation. The ferrites particles morphologies were observed by scanning electron microscope (SEM, JSM-5400). The magnetic properties of the ferrites were measured at room temperature using a vibrating sample magnetometer (VSM; 9600-1 LDJ, USA) in a maximum applied field of 10 kOe. From the obtained hysteresis loops, the saturation magnetization (*Ms*) was determined

III. RESULTS AND DISCUSSIONS

A mill scale sample with 70.1% total iron obtained from HADEED Saudi Iron & Steel Company (SABIC) was used in this study to synthesized magnesium ferrite through conventional ceramic rout as soft magnetic material for industrial applications. A series of experiments was carried out at different annealing temperatures ranging from 1000 to 1300℃ for 2 h to explain the effect of annealing temperature and Mg:Fe mole ratios (0.5, 0.55 and 0.65) on the formation of $MgFe_2O_4$ powder prepared using the conventional solid-state method. Fig. 1 showed the XRD patterns of $MgFe_2O_4$ from mill scale and magnesium oxide precursor with Mg:Fe mole ratio 0.5 thermally treated at temperatures 1000, 1100, 1200 and 1300℃ for calcination time of 2 h. From the results, It is evident that at Mg:Fe mole ratio 0.5, the formation of single-phase $MgFe_2O_4$ could not be obtained at this mole ratio and contains impurity peaks of α-Fe_2O_3 phase. At a temperature of 1000℃, the $MgFe_2O_4$ ferrite phase formed contained large amounts of impurity, which were due to the α-Fe_2O_3 phase. It can be observed that the presence of $MgFe_2O_4$ phase and hematite phase are nearly equal ratio. At 1100℃, the hematite phase was highly decreased while the $MaFe_2O_4$ was highly formed. This could be observed from the lowering of the peak intensities of hematite peak. Behind the annealing temperature 1100℃, the annealing temperature has a limiting effect on the formation of $MgFe_2O_4$. At annealing temperatures 1200 and 1300℃, a slight decrease in the hematite phase was observed. It could be also observed that the peak intensities for the ferrite phase were increased with the increasing of annealing temperature up to 1200^0C and slightly decreased at annealing temperature 1300^0C. These results indicated that the Mg:Fe = 0.5 did not led to the formation of single phase of $MgFe_2O_4$. This limiting effect of annealing temperature was due to the limiting connection between magnesium oxide and the iron oxide in the precursor at this mole ratio.

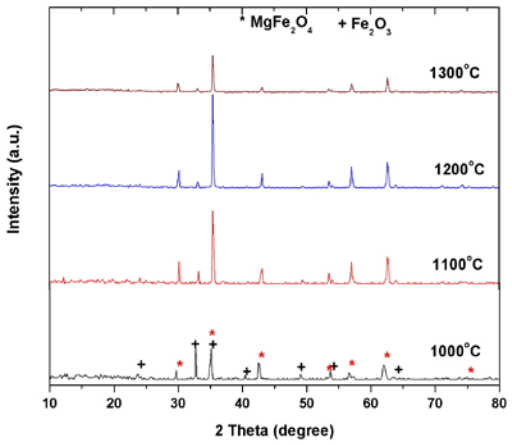

Fig. 1 XRD patterns of the $MgFe_2O_4$ powder produced at mole ratio of Mg:Fe = 0.5

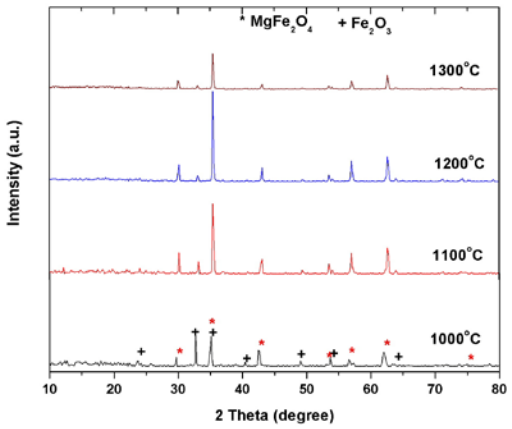

Fig. 2 XRD patterns of the MgFe2O4 powder produced at mole ratio of Mg:Fe = 0.55

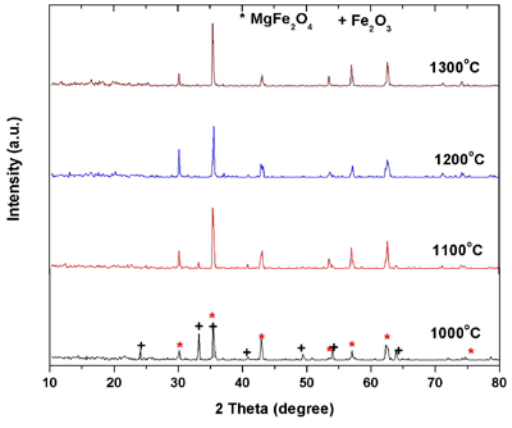

Fig. 3 XRD patterns of the MgFe2O4 powder produced at mole ratio of Mg:Fe = 0.65

Fig. 2 and 3 showed the XRD patterns of $MgFe_2O_4$ from mill scale and magnesium oxide precursor with Mg:Fe = 0.55 and 0.65, respectively, thermally treated at temperatures 1000, 1100, 1200 and 1300°C for calcination time of 2 h. As in Mg:Fe = 0.5, the $MgFe_2O_4$ ferrite phase formed contained large amounts of α-Fe_2O_3 phase at a temperature of 1000 °C and the presence of $MgFe_2O_4$ phase and hematite phase are almost equal ratios for both Mg:Fe = 0.55 and 0.65. This indicate that the Mg:Fe mole ratios had not strong effect on the formation of $MgFe_2O_4$ at low annealing temperature (1000^0C). As the annealing temperature increased to1100^oC, the formation of magnesium ferrite phase was highly enhanced for both the two Mg:Fe mole ratios. However, the Mg:Fe 0.55 did not led to the formation of single phase of $MgFe_2O_4$ at all annealing temperature (Fig. 2) while a single phase of $MgFe_2O_4$ was formed at annealing temperatures 1200 and 1300^0C for the precursor with Mg:Fe = 0.65 (Fig. 3). The peak intensities for the ferrite phase were increased with the increasing of annealing temperature up to 1200^0C and slightly decreased at annealing temperature 1300^0C for the two Mg:Fe mole ratios (Fig. 1-3).

The crystallite size of the produced magnesium ferrite phase for the most intense peak (3 1 1) was determined from the XRD data using the Debye–Scherrer formula. The crystalline size for the well-crystallized pure single $MgFe_2O_4$ phase was found to be increase by increasing the annealing temperature and depends on the Fe:Mg mole ratios. However, the crystalline sizes of 172 and 182 nm were obtained at 1200 and 1300 °C, respectively for Fe:Mg = 2:1.3.

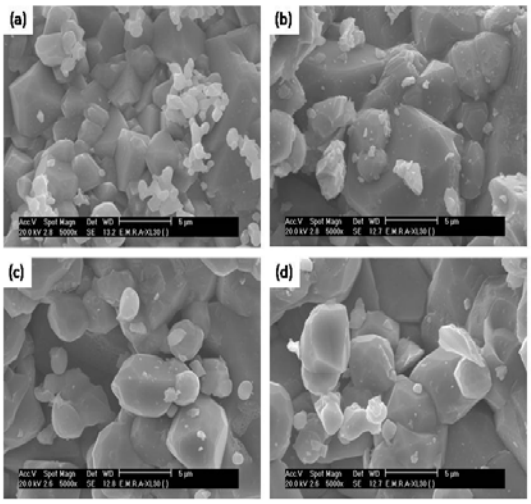

Fig. 4 SEM micrograph of the produced nanocrystalline MgFe2O4 powders prepared at: (a) Mg/Fe = 0.5 & 1200oC, (b) Mg/Fe = 0.5 & 1300oC, (c) Mg/Fe = 0.65 & 1200oC and (d) Mg/Fe = 0.65 & 1300oC

In order to investigate the influence of annealing temperature and Mg:Fe mole ratio on the morphology and microstructure of the prepared magnesium ferrite powder, further investigation was carried out by SEM and are shown in Fig. 4a-d. It is clear that there is an increase in grain size with raising annealing temperature. The SEM images of the powder synthesized from the mall scale and magnesium oxide with Mg:Fe = 0.5 and thermally treated at 1200°C for 2 h (Fig. 4a) showed irregular microstructures with spherical small particles in addition to the largest particles, indicating that the composition is insufficient for the complete formation of the structure. The presence of smaller grains can be attributed to no coarsened α-Fe_2O_3 existing in the annealed samples obtained at this Mg:Fe and this annealing temperature. The particles size of the formed ferrite was ranging from a diameter of 0.5 to 3.5 µm. For the powder with Mg:Fe = 0.5 and thermally treated at 1300°C (increase of annealing temperature), the ferrite powders possessed an uniform coarse structure with a well-clear crystalline microstructure containing a fewer numbers of spherical small particles as shown in Fig. 4b. It can be also observe that the grain size was larger than that observed at lower temperature .The average grain sizes for the powders annealed at 1300°C were about 1–6 µm. The clear and homogeneous microstructure become more pronounced for the sample with Mg:Fe = 0.65 annealed at 1200 and 1300°C, respectively, as shown in Fig. 4c and d. Moreover, the SEM micrographs showed that the spherical small particles were disappeared, which indicated that the Mg:Fe = 0.65 was sufficient to produce a single $MgFe_2O_4$ phase with homogeneous microstructure and a uniform size distribution with an average grain size of about 3 to 6 µm.

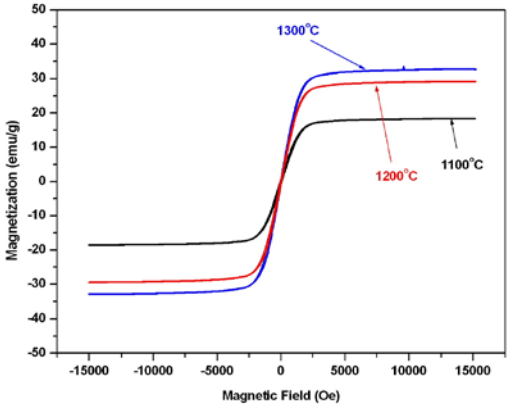

Fig. 5 Effect of annealing temperature on the M-H hysteresis loop of MgFe2O4 powders produced at mole ratio of Mg:Fe = 0. 5

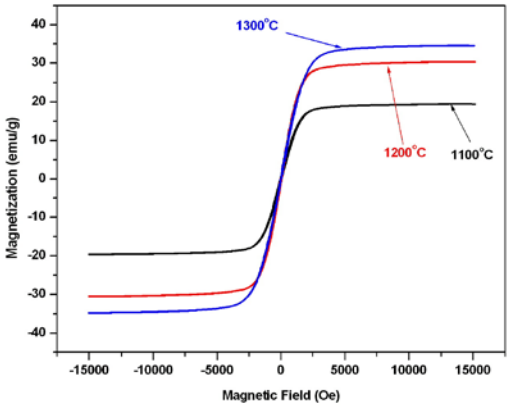

Fig. 6 Effect of annealing temperature on the M-H hysteresis loop of MgFe2O4 powders produced at mole ratio of Mg:Fe = 0. 55

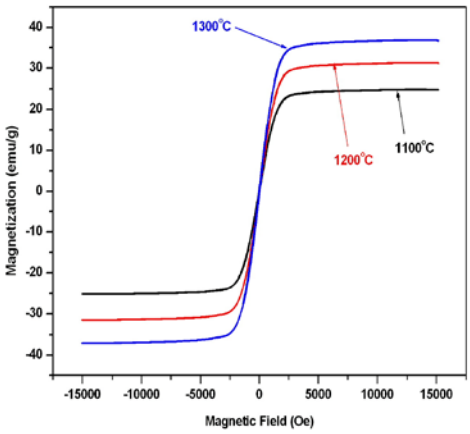

Fig. 7 Effect of annealing temperature on the M-H hysteresis loop of $MgFe_2O_4$ powders produced at mole ratio of Mg:Fe = 0. 65

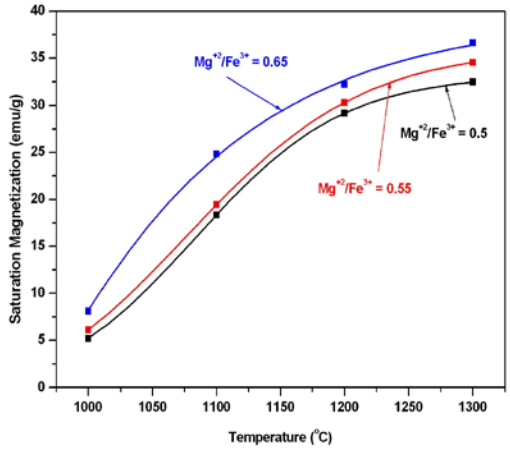

Fig.8 The saturation magnetization as a function of annealing temperature of MgFe5O8 for Mg/Fe =0.5, 0.55and 0.65 annealed for 2 h.

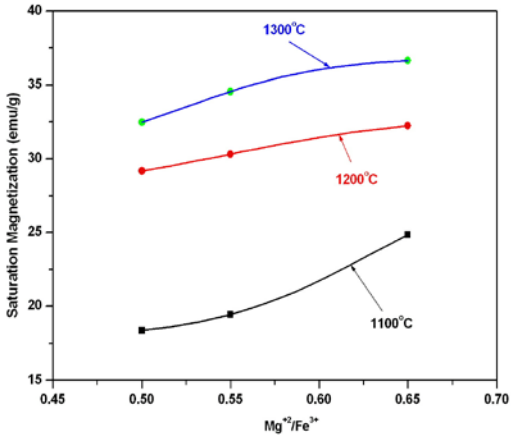

Fig.9 The saturation magnetization as a function of Mg/Fe mole ratio for annealing temperatures 1100-1300oC annealed for 2 h.

The magnetization of the produced magnesium ferrite powders was performed at room temperature under an applied field of 16 KOe and the hysteresis loops of the ferrite powders were obtained. Plots of magnetization (*M*) as a function of applied field (*H*) per Mg/Fe mole ratio and annealing temperature were shown in Figs 5 - 9. Figs. 5 - 7 showed the hysteresis measurements for the effect of annealing temperature (1100 -1300^{o}C) at Mg/Fe = 0.5, 0.55 and 0.65 respectively. Fig. 8 plotted the saturation magnetization as a function of annealing temperatures from 1100 to 1300^{o}C for all the Mg/Fe mole ratios (0.5, 0.55and 0.65) while Fig. 9 plotted the saturation magnetization as a function of Mg/Fe mole ratio for all the studied annealing temperature. In general, Fig. 5 and 7 indicated that the magnesium ferrite was a soft magnetic material due to the deviation from rectangular form and there very low coercivity and the magnetic properties of the prepared magnesium ferrites are strongly dependent on the Mg ion concentration and the annealing temperature. The results showed that the values of saturation magnetization of the Mg ferrite powders were increased by increasing the annealing temperature from 1100 to 1300^{o}C and which can be attributed to the increase in phase formation, sample grain size and crystalline sizes. The magnesium ferrite powders with Mg/Fe mole ratio 0.65 and annealed at 1300 C for 2 h exhibited an optimum saturation magnetization of 36.64emu/g. Such high saturation magnetization for Mg ferrite annealing at 1300◦C can be attributed to the high phase purity and well-defined crystallinity of $MgFe_5O_8$. Fig. 8 showed that the saturation magnetization increased steadily with increasing treatment temperature from 1100 to 1300^{o}C for the entire studied Mg/Fe mole ratios as results of increasing Mg ferrite formation. It exhibited a maximum value of magnetization at annealing temperature 1300^{o}C for 2 h. This is due to the presence of single phase of magnesium ferrite particles. The increase in the saturation magnetization by increasing the annealing temperature was due to the increase of phase purity and well-defined crystallinety of $MgFe_5O_8$. The saturation magnetization of the Mg ferrites powders increased continuously with the increase in Mg ion concentration up to Mg/Fe mole ratio 0.65 and at all annealing temperatures (1100-1300^{o}C) as shown in Figs. 9 and this can be attributed to the increase of the quantities of Mg ferrite formation. These results were in agreement with those observed in XRD results.

IV. CONCLUSIONS

Nanocrystalline magnesium ferrites were synthesized using secondary iron oxide "mill scale" produced from Hadeed Company (in KSA) which produced during the rolling of the steel slabs. The classical ceramic method was used for the preparation the magnesium ferrite. The results can be summarized as:

- A magnesium ion concentration was important to synthesize single-phase $MgFe_2O_4$ powder by economic ceramic route.
- A single- phase of nanocrystalline magnesium ferrite could not obtained a t Mg/Fe mole ratios 0.5 and 0.55 and contains impurity of α-Fe_2O_3 phase

A single phase of nanocrystalline $MgFe_2O_4$ was formed at the precursor with Mg/Fe mole ratios 0.65 at annealing temperature $\geq 1200^{o}C$.

- Samples that contains hematite as impurities showed irregular microstructures with spherical small particles
- The Mg/Fe mole ratios 0.65 was sufficient to produce a single $MgFe_2O_4$ phase with homogeneous microstructure and a uniform size distribution
- The nanocrystalline size of the prepared $MgFe_2O_4$ phase prepared by using co-precipitation methods was in the range of 170nm.
- The formed Mg ferrite powders had good magnetic properties with maximum saturation magnetization (36.64 emu/g) was achieved for the single phase at Mg/Fe mole ratio 0.65 and annealing temperature $1300^{o}C$.

REFERENCES

[1] E. C. Snelling, "Soft Ferrites, Properties and applications", Butterworth and Co. (Publishers) Ltd., London (1988).

[2] Alex Goldman, "Modern Ferrite Technology", 2nd Edition, Springer, (2005)

[3] A. Ataie, S.H. Manese, J. Eur. Ceram. Soc. 21 (2001) 1951.

[4] Y. Li, Q. Li, M. Wen, Y. Jhang, Y. Jhai, Z. Xie, F. Xu, S. Wei, J. Electr. Spectrosc. Relat. Phenom. 160 (2007) 1–6.

[5] P.Y. Lee, K. Ishizaka, H. Suematsu, W. Jiang, K. Yatsui, J. Nanopart. Res. 8 (2006) 29–35

[6] M. Tada, T. Kanemaru, T. Hara, T. Nakagawa, H. Handa, M. Abe, J. Magn. Magn. Mater. 321 (2009) 1414–1416.

[7] G. Zhang, C. Li, F. Cheng, J. Chen, Sens. Actuators B. 120 (2007) 403–410.

[8] M.A. El Hiti, A.I. El Shora, S.M. Hammad, Mater. Sci. Technol. 13 (1997).

[9] T. Nakamura, Y. Okano, J. Phys. IV Fr. 7 (C1) (1997) 101.

[10] J. Szekely, ISIJ International, 36 (1996) 121.

[11] N. Leclerc, E. Meux, J.M. Lecuire, Hydrometallurgy, 70 (2003) 175–183.

[12] K. Thakur, BHU, Varanasi, India (200) 187.

[13] U. S. Yadav, B.K. Das, A. Kumar, Proceedings of 6th southern hemisphere meeting on mineral technology, Brazil (2001) 719.